3D multiple point geostatistical simulation of joint subsurface redox and geological architectures

Rasmus Bødker Madsen[1], Hyojin Kim[1], Anders Juhl Kallesøe[1], Peter B.E. Sandersen[1], Troels Norvin Vilhelmsen[2], Thomas Mejer Hansen[2], Anders Vest Christiansen[2], Ingelise Møller[1], Birgitte Hansen[1]

5 [1]Geological Survey of Denmark and Greenland, Groundwater and Quaternary Geology Mapping, Aarhus, 8000, Denmark
[2]Aarhus University, Department of Geoscience, Aarhus, 8000, Denmark

Correspondence to: Rasmus Bødker Madsen (rbm@geus.dk)

Abstract. Nitrate contamination of subsurface aquifers is an ongoing environmental challenge due to nitrogen (N) losses from intensive N fertilization and management on agricultural fields. The distribution and fate of nitrate in aquifers are primarily

10 governed by geological, hydrological and geochemical conditions of the subsurface. Therefore, we propose a novel approach to model both geology and redox architectures simultaneously in high resolution 3D (25m x 25m x 2m) using multiple point geostatistical simulation (MPS). Data consists of 1) mainly resistivities of the subsurface mapped with towed transient electromagnetic measurements (tTEM), and 2) information of lithology and redox conditions obtained from the borehole observations at point scale interpreted from the geological descriptions and colors of sediment samples, and chemistry analyses

15 of water samples. The conceptual understandings of the geological and redox architectures of the study system were introduced to the simulation as training images. These data were combined with detailed soil maps and digital elevation models to identify main geological elements defined as volumes within the subsurface. From a geological perspective, these data are considered independent from each other in terms of formation. This approach became computationally attractive by simulating smaller geological elements individually instead of the entire catchment. The final realizations were stitched together using simulations

20 of the individual geological elements, resulting in an ensemble of realizations representing a quantification of the uncertainty for the given setup. The joint simulation of geological and redox architectures, which is one of the strengths of the MPS simulations compared to other geostatistical methods, secures that the two architectures in general show coherent patterns. Despite the inherent subjectivity of interpretations of the training images and geological element boundaries, they enable an easy and intuitive incorporation of qualitative knowledge of geology and geochemistry in quantitative simulations of the

25 subsurface architectures. Altogether, we conclude that our approach effectively simulates the coherent geological and redox architectures of the subsurface that can be used for hydrological modelling with N-transport, which may be fundamental to better understanding of the nitrogen (N) retention of the subsurface and to future more targeted regulation of agriculture.

1 Introduction

30 The escape of reactive nitrogen (N) from agricultural soils results in adverse environmental and human health impacts (Schullehner et al., 2018; Temkin et al., 2019), including eutrophication of freshwater and estuarine ecosystems and nitrate contamination of groundwater and drinking water (Hansen et al., 2017 & 2019). In Denmark, since the 1980s N-regulations of intensive agriculture at national or regional scales have succeeded in lowering the N-impact on the aquatic environment (Dalgaard et al., 2014; Hansen et al., 2017). However, further actions are still required to improve the state of the aquatic

35 ecosystems to meet the requirements of e.g. the EU Water Framework Directive (Kallis and Butler, 2001). Moreover, this has to be achieved in a cost-effective manner for the society and the agricultural industry. This creates a demand for new knowledge and new solutions for more efficient future N-regulation of the agricultural sector both in Denmark and in other countries with intensive agriculture. The proposed direction is to tailor the N-regulations depending on the site-specific conditions at field level, called targeted N-regulations. The targeted N-regulations require detailed knowledge about the subsurface

40 hydrogeological and biogeochemical conditions because nitrate, which is the dominant form of N in aquatic environments, is transported predominantly with water flow and undergoes reduction in the typical deeper reduced aquifers. Thus, it has now become increasingly important to have detailed knowledge of the subsurface geology and redox architectures.

In a simple case with only vertical infiltration, nitrate concentrations in aquifers decrease with an increasing depth along three

45 sequential redox zones (Kim et al., 2019; Wilson et al., 2018):

1) Oxic zone: Nitrate conditions are equal to the leaching from the soil because of the oxic conditions preventing reduction

2) Nitrate reducing zone: Nitrate decrease with increasing depth due to ongoing reduction of nitrate

3) Reduced zone: Nitrate free zone due to complete reduced redox conditions

50 The redox conditions of the subsurface has been widely investigated using various approaches focusing on different redox sensitive chemical compounds such as nitrate, iron, sulphate, pyrite, organic matter, arsenic, uranium, and some organic contaminants: 1) process-based approaches (e.g. (Abbaspour et al. (2007); Hansen et al. (2014a,2016a); Lee et al., (2008)), 2) geostatistical methods (e.g., Kriging; Ernstsen et al. (2008); Goovaerts et al. (2005); Lin, (2008)) and 3) machine learning (Close et al., 2016; Koch et al., 2019; Nolan et al., 2015; Ransom et al., 2017; Rosecrans et al., 2017; Tesoriero et al., 2015;

55 Wilson et al., 2018). However, many of these approaches require large sets of data of especially groundwater chemistry, and it is costly and time consuming to collect sufficient volumes of data. Furthermore, ancillary data to spatially extrapolate the water chemistry, for instance soil types, topography, land use, surface slopes, only provide information about the near surface conditions (i.e., topsoil layer); therefore, predicting the redox conditions below the topsoil layer using these data may be inadequate. Particularly under geologically heterogeneous settings such as glacial terrain, the redox architecture can be

60 complex (e.g. Kim et al. (2019)) with many shifts in redox state with depth at the same location. Upscaling of the point scale measurements of redox conditions into the 3D space thus requires detailed spatial information of the subsurface geological architecture.

In Denmark, the uppermost 100 to 200 meters of the subsurface generally consists of unconsolidated sediments reworked or

65 generated by glacial processes, making the subsurface architecture complex (Høyer et al., 2015; Jørgensen et al., 2015). Through the National Groundwater Mapping Program, Denmark is extensively covered with airborne electromagnetic measurements (AEM) (Møller et al., 2009; Thomsen et al., 2004) and together with borehole data, 3D geological mapping of Denmark has been carried out as cognitive modeling (see e.g. Høyer et al., 2015). In cognitive modeling, an experienced geologist combines all available subsurface data (e.g. boreholes, electromagnetic data, and seismic data) with preexisting

70 geological background knowledge and performs interpretations through either manual (e.g. Jørgensen et al., 2013) or semi-automatic approaches (e.g. Gulbrandsen et al., 2017; Jørgensen et al., 2015). Complex geological settings, however, pose a

challenge for 3D modeling and interpretations between geological point data may lead to large uncertainties (Wellmann and Caumon, 2018).

75 The subsurface information itself is attributed to uncertainties such as measurement errors (Malinverno and Briggs, 2004), errors from using approximate physics (Hansen et al., 2014b; Madsen and Hansen, 2018), bias from interpolation methods (Wellmann and Caumon, 2018), and processing errors when handling geophysical data (Claerbout et al., 2004; Madsen et al., 2018; Viezzoli et al., 2013). Even geological knowledge cannot be considered uncertainty free (Bond, 2015; Lindsay et al., 2012; Sandersen, 2008; Wellmann et al., 2018). In fact, subjective biases are accepted as one of the weak points of cognitive 80 geological modeling (Bond, 2015; Wycisk et al., 2009). Generally, it is therefore difficult to fully incorporate uncertainties related to the subsurface information in cognitive modelling, and even more difficult to propagate these uncertainties through to subsequent analysis such as hydrological modelling.

In recent years, some studies have adapted geostatistical simulation methods for geological mapping of the substratum in order 85 to quantify and possibly account for some of these uncertainties. A few examples exist of multiple-point geostatistical simulation (MPS) utilized for mapping 3D geology with AEM data (Barfod et al., 2018; He et al., 2014b; Høyer et al., 2017; Jørgensen et al., 2015; Vilhelmsen et al., 2019). However, AEM data provide structural information of the deeper subsurface (100-200 m deep) at a coarser resolution (Sørensen and Auken, 2004), and hence may not be adequate to provide structural information for simulations of N-transport at catchment level occurring mainly within the upper 30 m. A newly developed 90 towed transient electromagnetic method (tTEM) (Auken et al., 2019) provides data at much higher resolution but with a lower penetration depth than AEM. tTEM is, therefore, ideal for high-resolution mapping when focusing on the uppermost 50 to 70 m of the subsurface. None of the previous studies has investigated the geological and redox architecture simultaneously although these two are related and sometimes coevolved (Grenthe et al., 1992; Hansen et al., 2016a; Wilkin et al., 1996; Yan et al., 2016).

95

The development of redox zones in the subsurface is dependent of several factors including 1) infiltration of atmospheric oxygen in geologic time; 2) anthropogenic leaching of nitrate; 3) the amount and reactivity of geogenic reducing minerals as pyrite or organic matter; and 4) the hydrogeological flow conditions. We propose a novel way to combine the available information about hydrogeology and redox conditions (boreholes, electromagnetic data, geological maps and digital elevation 100 maps) and quantify uncertainty in modeling and data using geostatistical simulation. We specifically use MPS simulation to describe the spatial uncertainty in our models through a series of possible realizations of the subsurface (Mariethoz and Caers, 2015). Using a bivariate training image (TI) of both geology and redox, we jointly simulate both redox and geology to ensure these will be consistent in the realizations. TIs are created using expert knowledge combined with the available data to directly incorporate prior expert geological information. In addition to our proposed efforts of combining redox and geology modeling, 105 we have also utilized data and geological knowledge to subdivide the simulation volume into smaller volumes based on different geological characteristics and the depositional environment. We refer to such smaller volumes as 'geological elements'. Individual TIs are created with cognitive voxel modeling for each geological element so that they can be simulated independently and subsequently stitched together. This is computationally attractive since both training images and simulation grids shrink in size in contrast to simulating the entire volume in a single operation. Geological interpretation of the 110 depositional environment and the age of the sediments will help create an event chronology that supports the independence between the geological elements.

The aim of this paper is to demonstrate and review the proposed methodology focusing on strengths and weaknesses. This is, to our knowledge, the first study of simultaneous modeling of geology and redox architectures in a geostatistical high-

115   resolution 3D model. This may be fundamental to better understanding N retention within the subsurface and important for
future more targeted N regulation and management of agriculture for protection of vulnerable surface waters and groundwater.
Thus, providing stakeholders with a powerful tool based on integrated expert knowledge and quantified structural uncertainty
through probabilistic predictions of the complex interplay between redox and geological architecture.

2 The study area

120

The study area is a small Danish agricultural first-order hydrological catchment to Horndrup Bæk called LOOP3 with an area approximately 550 ha. The area is located at the Jutland peninsula in Denmark, with a coastal temperate climate (Figure 1). The dominant soil types are classified as sand-mixed clay (70%) and clay sand (24%). Forest accounts for 18% of the catchment area, the rest being used for agricultural purposes except for a limited area taken up by buildings and roads. The catchment has

125 been part of the Danish National Environmental Monitoring Program since 1989 aiming at evaluating the effect of the Danish N-regulation of agriculture on the aquatic environment (Hansen et al., 2019). During the last almost 30 years, the N concentrations in soil water, drainage, shallow groundwater and streams have been measured regularly at several stations in the agricultural fields (Blicher-Mathiesen et al., 2019). Therefore, the site is ideal for testing new subsurface mapping techniques of geological and redox architectures.

130

The study area is located in a hilly glaciated landscape in the eastern part of Jutland just east of the highest point in Denmark (Figure 1). The highest elevations reach 170 meters above sea level (m a.s.l.) in the southwestern part and slopes down to around 40 m a.s.l. in the northeast (Figure 1a). To the north of the study area, a system of open tunnel valleys forms a low-lying area with several lakes. The catchment is dominated by glacial till deposits from the latest glaciation and the orientation

135 of the hills generally show former ice push directions from the northeast. In the lowest parts of the terrain, occurrences of meltwater sand are also found. Occurrences of postglacial freshwater deposits can be found locally in smaller topographical lows (Jakobsen et al., 2011). Several buried valleys have been mapped outside the study area (Sandersen and Jørgensen (2016); www.buriedvalleys.dk (2020); Figure 1). The buried valleys were formed as elongated tunnel valleys underneath the ice sheets, they are generally between 1 and 2 km wide and some of them have depths of more than 100 m (Jørgensen and Sandersen,

140 2006; Sandersen and Jørgensen, 2017). These valleys are generally filled with younger Quaternary sediments. In this region, the valleys mostly have two preferred orientations, one around WNW-ESE/NW-SE and the other around SW-NE/WSW-ENE (Figure 1), with the first mentioned clearly visible in the present-day topography.
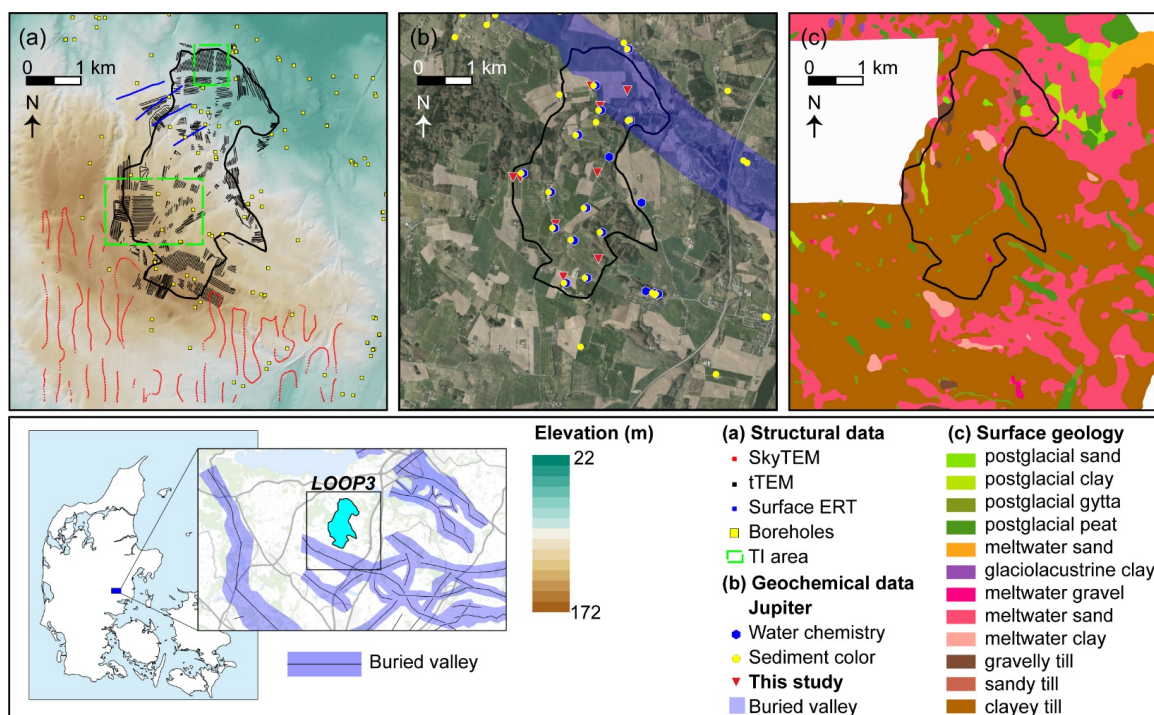
145 **Figure 1: The study area and available data, where a) display digital terrain model, geophysical data and outlined TI areas, b) an orthophoto and geochemical data, and c) soil map (1 m below surface (Jakobsen et al., 2011)). Insets with map of Denmark and regional view of the study site with mapped buried valleys (www.buriedvalleys.dk (2020)).**

3 Materials

Some data are specifically gathered for this study (tTEM and new boreholes, see Figure 1) while other existing data are freely available through the Danish shallow borehole database "Jupiter" (Hansen and Pjetursson, 2011) and the Danish geophysical

150 database for onshore data "GERDA" (Møller et al., 2009). All available data are shown in Figure 1 along with the terrain and outline of the study area.

3.1 Geological and topographical data

The digital elevation map presented in Figure 1a is available from Styrelsen for Dataforsyning og Effektivisering (2016). The elevation map is resampled on a 25m x 25m grid such that adjustment with interpreted surfaces is seamless.

155 The geological surface map (Figure 1c) of the surficial cover of Denmark is compiled from small pristine sediment samples collected at c. 1 m depth using a so-called spear-auger. The mapping geologists interpret the origin and type of the sediment in the field and classify a sediment-type following the current terminology described by Jakobsen et al., (2011). Samples are taken with a distance of 100-200 m to map the transitions between the different sediment types. Afterwards the soil-symbols are transferred to a master map, contoured and color-coded resulting in a geological map sheet on a scale of 1:25.000 with a

160 resolution of ± 100 m (Figure 1c, https://eng.geus.dk/products-services-facilities/data-and-maps/maps-of-denmark/ (2020))

Borehole lithological information (Figure 1a) is gathered from the Jupiter database to which lithological sample descriptions have been reported since 1912. The borehole lithological samples are described and interpreted by geologists following standards outlined by Gravesen and Fredericia (1984), including interpretation of depositional environment and

165 chronostratigraphy and thereby resulting in sediment types similar to those used in the geological mapping.

In our study site, total 25 specific sediment types are found in borehole descriptions and on the geological surface map combined. To lower the number of variables in the geostatistical modelling and in later hydrological simulations, the sediment types are grouped into five categories focusing on their hydrological properties (Table 1). The partly organic postglacial

170 sediments may show variable hydrological properties. However, they are hugely important in terms of redox potential; therefore, they are categorized in one group.

Table 1: Lithology groups in the study area. The five bold face groups are used in the geostatistical simulation. The sediment-type abbreviations in the right column represent the Danish sediment characterization standards.

Lithology groups – study area		
no.	*Group name*	*Soil type*
1	Clay till	ML, (L)
2	Meltwater sand/gravel	DS, DS-DG, DG, G, S, TS, (O)
3	Meltwater clay/silt	DL, DI, DV, (FL)
4	Sandy till	MS, MG
5	Postglacial (partly org.)	FP, FT, FS
6	Pre-Quaternary clay	LL, SL, (GL)
7	Unknown	B, U, X

3.2 Geophysical data

The tTEM (on land) and SkyTEM (airborne) are transient electromagnetic systems used for mapping subsurface resistivity variations (Auken et al. 2019, Auken and Sørensen 2004). The SkyTEM system carries the instrument, transmitter loop and receiver coil in a sling load under a helicopter and is designed to map resistivity to several hundred meters depth. The tTEM system applies the transient electromagnetic method in an offset-loop configuration which for the present study is configured using a 2 m by 4 m transmitter loop and a receiver coil in a distance of 9 m, towed by an all-terrain vehicle (Auken et al., 2019). The tTEM system is designed to resolve resistivity from 2-3 m depth to c. 70 m depth. Processing and inversion of tTEM data follow in general the scheme for SkyTEM, described by Auken et al. (2009). The inversion of the data is based on local 1D forward responses and spatial constraints between the model parameter forming a pseudo 3D model space (Auken et al., 2015; Viezzoli et al., 2008).

The tTEM dataset has been collected in 2018. Although the coverage is rather patchy (< 50 % of the model area in Figure 1a), it provides valuable information on the geological setting. The final tTEM information used in the geostatistical modelling is the pseudo 3D model space moved to the closest grid node. Together with borehole lithological logs, tTEM represents the basis for modelling the geology. A few deep boreholes are used for the correlation between resistivities and lithologies.

Although located outside the study area, the SkyTEM-data (Figure 1a) adds valuable information on the geological connections to neighboring areas. A small survey of surface electrical resistivity tomography (ERT) (e.g. Loke et al. (2013)) gathered from the GERDA database supplements the tTEM survey in the northern part of the study area.

3.3 Geochemical data

The sediment colors and groundwater chemistry were the main input data for the redox condition interpretations. These data were extracted from the Jupiter database and the 9 new boreholes that were drilled in this study (Figure 1b). In this study we use both sediment colors and redox sensitive water compounds to define the redox conditions of the aquifer. The benefit of using the two types of data is that they provide independent measurements of redox conditions.

In Denmark, sediment colors have been widely used to interpret redox conditions (Ernstsen and von Platen, 2014; Hansen et al., 2016a; Kim et al., 2019) and these data are publicly accessible in the Jupiter database. Red, orange, yellow and combinations of these colors represent oxic conditions and gray, olive and blue colors represent reduced conditions. Mixed colors between oxic and reduced colors (e.g., yellowish gray) are defined as N-reducing conditions. Within the catchment boundary, the sediment color data were available at 14 boreholes in the Jupiter database and for the 9 new boreholes.

The concentrations of redox sensitive compounds in groundwater and soil water samples, mainly dissolved oxygen (DO), nitrate, iron, and sulfate, were used for the redox interpretation in this study as well (Hansen et al., 2017 & 2019). Based on water chemistry, oxic is defined by DO greater than 1mg/L, N-reducing is DO less than 1mg/L and nitrate greater than 1mg/L, and reduced is both DO and nitrate below 1 mg/L and iron greater than 0.2 mg/L. The water chemistry data were available at 22 locations (13 in the Jupiter database and 9 in this study).

4 Methods

4.1 MPS modelling

In this paper, we adopt a multiple-point geostatistics (MPS) simulation approach for quantifying the spatial uncertainty of the
215 subsurface. Geostatistical simulation generally provides a way of quantifying the spatial uncertainty through different possible
realizations of the subsurface architecture. These realizations are generated using stochastic modeling that accounts for the
spatial dependency between the model parameters. We choose MPS simulation over e.g. a two-point geostatistical approach
because it is generally more capable of producing realizations with geological realism in terms of correlation and coherency
of geological features (Mariethoz and Caers, 2015). Effectively reproducing coherent layers is key for a successful subsequent
220 hydrological modeling. The expected subsurface variability is portrayed in one or more training images (TIs). MPS simulation
is then able to utilize these TIs to generate different realizations of the portrayed subsurface through a stochastic sampling
process. In total, these realizations, stemming from the MPS algorithm plus TI, together represent the quantified prior
information of the system. In our case, the intuitive aspect of a TI, as opposed to a mathematical prior, is helpful for
collaboration between mapping experts and geostatisticians.
225

Many MPS algorithms exist today (Gravey and Mariethoz, 2019; Guardiano and Srivastava, 1993; Hansen et al., 2016b;
Hoffimann et al., 2017; Mariethoz et al., 2010; Straubhaar et al., 2011; Strebelle, 2002; Tahmasebi et al., 2012). In the current
study we use direct sampling (Mariethoz et al., 2010) as implemented in the software package DeeSse (Straubhaar, 2019). The
main reason is due to its ability to utilize a bivariate training image that allows for joint simulation of geology and redox.
230

Simulations can be forced to match observational data creating conditional realizations (Chilès and Delfiner, 2012; Journel
and Huijbregts, 1989). Additional data not portrayed in the TI enters the simulation setup as either hard or soft data. Hard data
corresponds to information not allowed to change between different realizations and is placed directly in the simulation grid.
Information from some boreholes can often be considered as hard data because it is fixed in space and can have a relatively
235 high resolution and accuracy. Hard data, in most cases, offers the first conditional nodes and patterns to be matched during
simulation, depending of course on the number of conditional points used. Consequently, hard data usually plays a significant
role in lowering the entropy of the final simulations. If data is not reliable enough (too uncertain) to be deemed hard data, they
can instead be treated as uncertain information (soft data), quantified through probability distributions. In DeeSse, a penalty
proportional to the soft data mismatch is applied when searching for a matching event in the TI to incorporate this information
240 in the final simulations (Mariethoz et al., 2015).

4.2 Ensemble statistics

We introduce the mode and entropy as summary statistics for the ensemble of possible models of the subsurface. For a discrete
probability distribution, the mode represents the most probable category in each voxel. The entropy, H, of a discrete probability
distribution with K outcomes is explicitly calculated as (Shannon, 1948):
245

$$H = -\sum_{k=1}^{K} \log_K \big(p(k)\big)\, p(k), \tag{1}$$

where $p(k)$ is the probability of the kth outcome. In our case, the entropy is calculated in each voxel where $p(k)$ is the number
of times a certain category appears in the realizations divided by the number of realizations. The entropy reveals insights to
250 the variability and hence the certainty of a specific outcome of each voxel. For H=0 we have full certainty of the voxel category
and conversely for H=1. The mode and entropy are hence comparable to the mean and variance in Gaussian statistics.

5 Modelling setup

255   In the following, we present the methodology progressing through the modeling workflow of the study area. The workflow consist of three phases: 1) Preparing input data, 2) data analysis and setup including delineation of geological elements, construction of training images, preparing hard and soft data as well as setting up the simulation grid, and 3) run MPS simulations. A schematic overview of the workflow is seen in Figure 2. The following sections primarily describe phase 2.
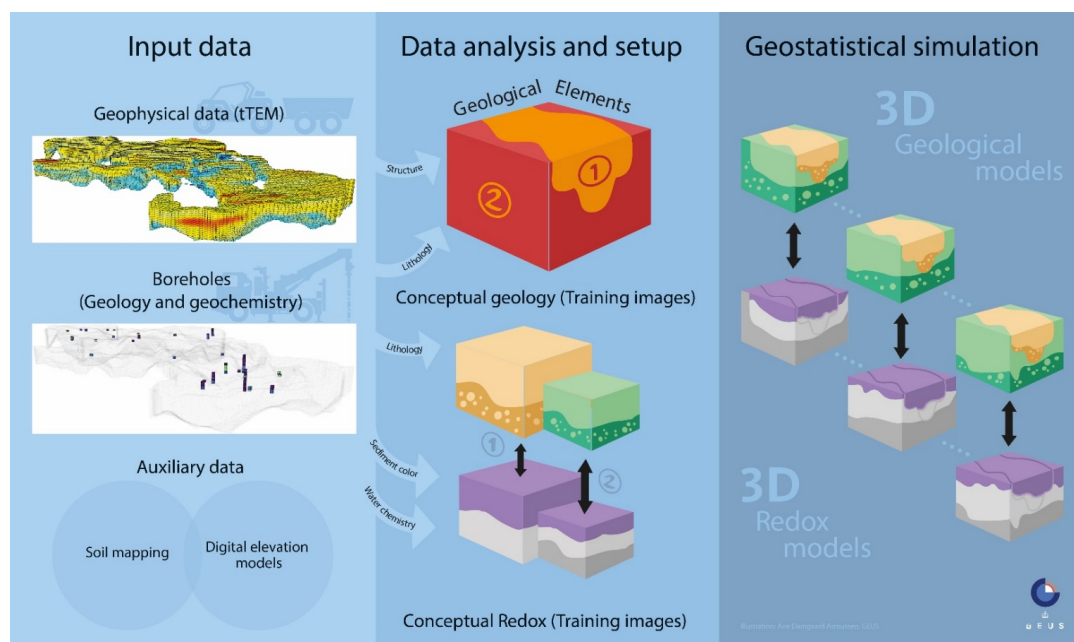
Figure 2: Schematic overview of the proposed workflow from input data (left) through data analysis and simulation
260   **setup (middle) and geostatistical simulation (right).**

5.1 Simulation grid

The simulation grid is discretized with a voxel resolution of 25m x 25m x 2m. The digital elevation model constitutes the top of the simulation grid, whereas both the bottom boundary and the internal subdivision into subvolumes are delineated by the geological elements (see below for details). The resulting simulation grid is shown in Figure 3b and the total number of voxels

265   in the simulation grid is listed in Table 2.

Table 2: Summary of number of voxels for simulation grid and TIs. The relative sizes of the TIs are calculated as the ratio between the number of voxels in the TI and the number of grid voxels.

	Number of voxels	Number of voxels in TI	Relative size of TI
Quaternary sequence (Element 1)	143698 voxels	54258 voxels	37.76%
Buried valley (Element 2)	57015 voxels	12449 voxels	21.83%
Total	200713 voxels	66707 voxels	33.24%

5.2 Geological elements

The geologist interprets and delineates the geological elements of the subsurface using the geological, geophysical and topographical input data. Three distinct geological elements are identified in the study area, see Figure 3a; (1) An upper Quaternary succession of sediments having an erosional boundary to the pre-Quaternary sediments below, (2) A large, deeply eroded, buried tunnel valley and (3) Pre-Quaternary Paleogene clays defining the bottom of the groundwater system. The simulation grid is chosen to include only the Geological Elements 1 and 2 (see Figure 3b). The third geological element, the Paleogene clay, constitute a thick non-penetrable layer, and as its top defines the lower hydrological boundary of the area, geostatistical simulation has not been performed on this geological element. We find it reasonable to do so because the Paleogene clays are homogeneous and very thick. This type of clay is generally found as a good electrical conductor in Denmark, and because the TEM method is sensitive to good conductors, the depth to the top of the layer can be determined with low uncertainty (e.g. Danielsen et al. (2003)). The Paleogene clay surface is hence trivial to acquire from the tTEM data, as long as it can be found within the depth of investigation of tTEM method (Vest Christiansen and Auken, 2012). Furthermore, in the study of Barfod et al. (2018), Paleogene clays were given a discrete value in the MPS simulation but showed only little variability in the spatial extent.

We assume independence between the two uppermost geological elements because they appear to represent different geological events. The buried valley to the north is apparently incised into both the Quaternary sequence and the pre-Quaternary clay below, and the infill is clearly different compared to the Quaternary sediments to the south. The buried valley (Geological Element 2) has a more complex infill with individual layers of limited extent compared to the Quaternary layers of Geological Element 1, which show less complexity and more pronounced stratification. The geological events that formed each element are therefore considered different although they contain the same lithology groups, and this justifies the assumption of independence from a geological point of view. The buried valley to the north takes up roughly a quarter of all voxels whereas the Quaternary sequence occupies the main part of the simulation grid (Table 2).

295
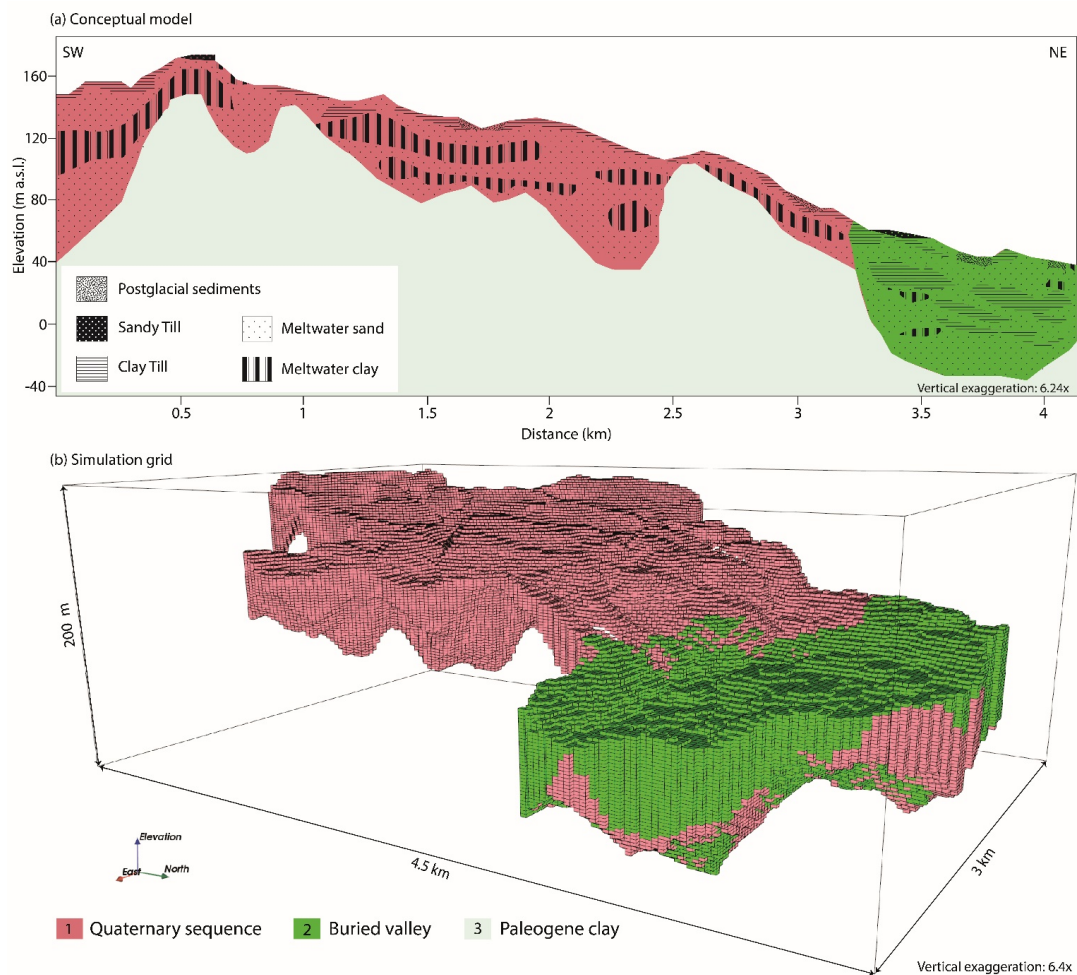
Figure 3: a) Conceptual drawing of SW/NE profile through the study area. b) Simulation grid.
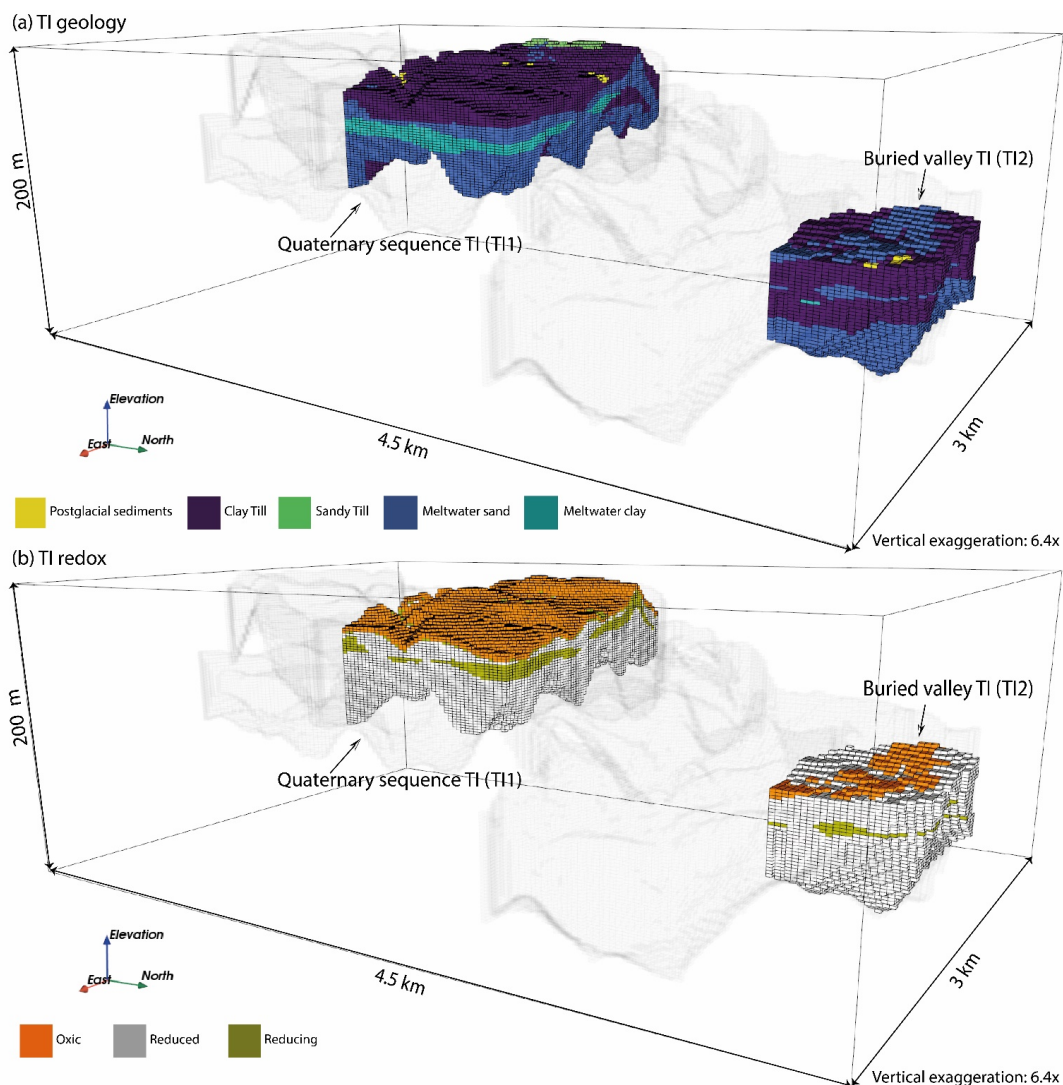
Figure 4: Training images. a) Geology TIs overprinted on the simulation grid. b) Redox TIs overprinted on the simulation grid.

5.3 Training images

The training images (TI) providing information about the geology and redox conditions within the geological elements are designed in a sequential workflow (Figure 2). At first, two geology TIs are generated, one within each of the two geological elements. The first step is to appoint a smaller part of the simulation area for detailed geological characterization and interpretation using a voxel modelling approach, see Figure 4a. The lithological population of the voxels is based on the conceptual understanding of the geological event chronology, glacial processes forming the area, and an interpretation combining borehole information and the spatially distributed geophysics (tTEM). The criteria for TI area selection in this specific study are dense data coverage of geophysics and availability of boreholes with good quality lithological logs. Likewise, the TI section needs to represent the expected variability in geology, both in vertical and horizontal extent. In reality, it is not possible to capture the total variability and heterogeneity in the TI space, but the important features must be represented. We only expect the "sandy till" group (light green) to appear at the surface of the buried valley (Element 2). To accommodate this the sandy till is not present in the TI for simulation.

The geological training images are translated into redox training images by integrating geochemical and water chemistry data (Figure 4b). Note that in case of the buried valley element, there are no boreholes with sediment color descriptions within the

315   catchment. Therefore, boreholes from the extension of the buried valley structure outside of the catchment area were selected, and the sediment color data were extracted from the Jupiter database. Based on the criteria for the redox interpretation outlined in the section on geochemical data, the borehole information and water chemistry data were translated to redox conditions, allowing the estimation of redox profiles with depth for sand and clay for each geological element.

320   This sequential workflow ensures consistency between the two training images in the joint simulation of the two variables. Approximately one-fourth of TI1 reaches outside of the study area whereas the whole of TI2 is located within. We intentionally do this in order to ease the construction of the TIs. TI1 is about one third of the size of the element 1 and that of TI2 is one fifth of element 2 (Table 2).

5.4 Conditional data

5.4.1 Hard data

The geological surface map and the borehole data (both lithology and redox) were treated as hard data in the simulation grid and are shown in Figure 5. The redox conditions are grouped into the three main redox categories; oxic, nitrate reducing, and reduced. The wells indicate that the area is dominated by reduced conditions. Oxic conditions are mainly present in the upper

330   meters of the simulation domain, and only one well displays the reverse trend with an oxic part below reduced conditions due to heterogenous geology.

The soil types that were grouped into lithologies (Table 3) were placed at the top voxel in the simulation grid, corresponding to the surface. We do not explicitly use the entire geological map as hard data. The borders between the lithology polygons of the soil map were originally delineated based on soil samples, geomorphology, and topography (Jakobsen et al., 2011). In

335   general, it means that the closer you are to the center of a polygon, the more certain you are of the correct lithology. Conversely, the boundaries between polygons represent the least certain parts of the map. A buffer zone is adapted between the polygons to express the uncertainty of the geological surface map. The buffer zone is simply created by checking all neighboring voxels for each voxel in the surface map. If the current voxel shares a value with all surrounding voxels it is likely situated safely

340   within a polygon and is kept as hard data. Conversely, if one of the neighboring voxels provides a mismatch, the current voxel is likely close to a polygon boundary and is not included as hard data. Alternatively, a negative buffer around each soil unit could be adapted.

5.4.2 Soft data

As mentioned above, we use the geological surface map (Figure 1c) as a soft data indicator of lithology in the buffer zone.

345   Geological complexity is one of the main drivers of uncertainty in geological mapping along with the amount, quality and spatial distribution of data (Keefer, 2007). Accessibility is an important factor to consider in terms of both amount and spatial distribution of data (Keaton and Degraff, 1996). In Denmark, however, neither terrain nor private property poses a major issue when mapping surface geology. On the level of investigation, the geology in the study area is relatively simple, alleviating some of the uncertainty due to complexity. The main source of uncertainty in the surface geology maps comes from

350   interpretations of sediment types from the small samples and the final shape and size of polygons. We generally consider the surface geology very certain data and thus provide all values 0.8 probability of being true. The last 0.2 probability is split equally between the four other lithologies and hence reflect the uncertainty level of misinterpretationsRegardless, because

much of the geological surface map is used directly as hard data, the quantified uncertainty only affects the buffer zone as outlined earlier.

355
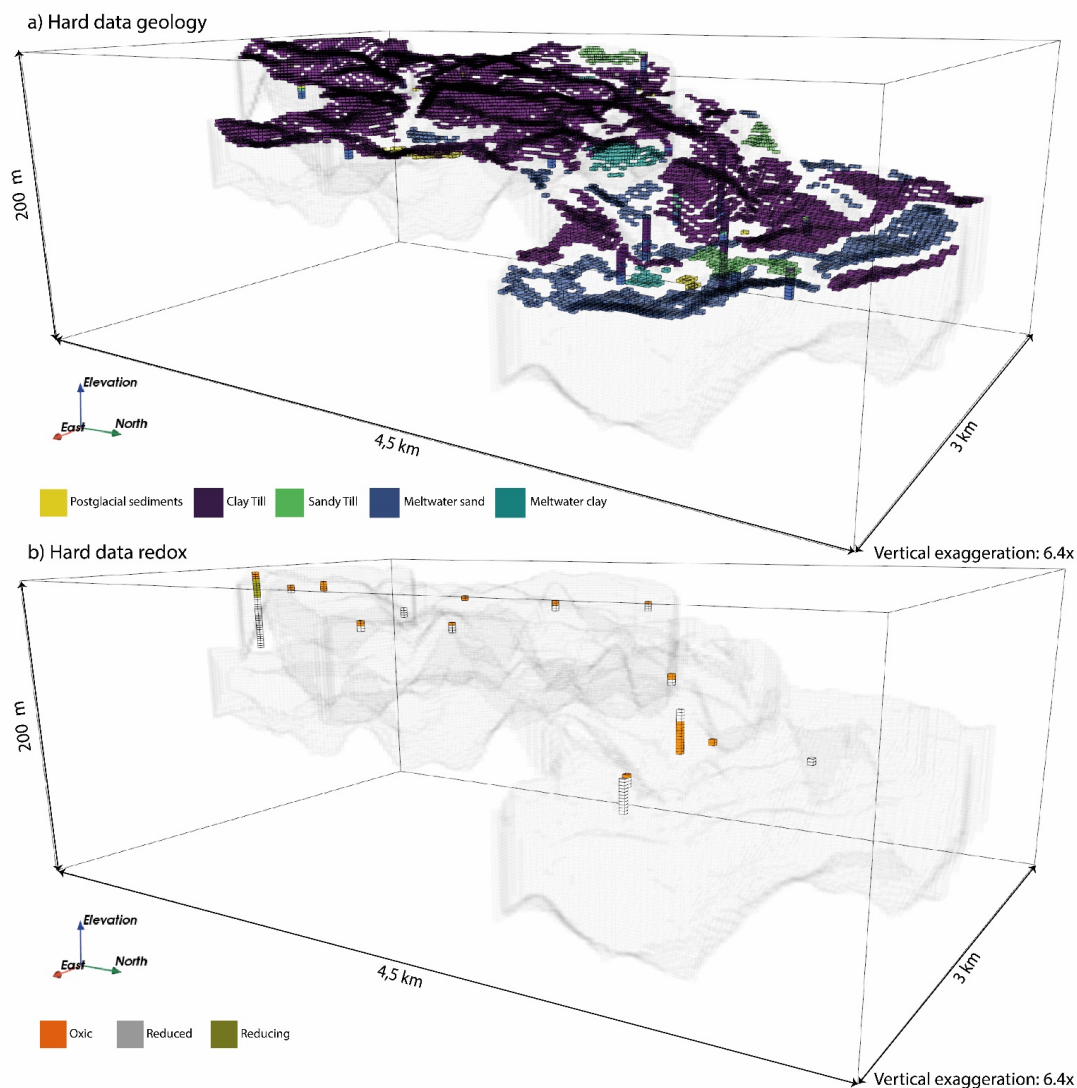
Figure 5: a) The geology surface map along with the geology wells placed on the simulation grid. Right: The redox wells on the simulation grid.

For the redox domain, we translate the geological surface map to soft redox data. Lithology and water saturation may be two

360   key factors on determining redox conditions in soils by regulating rates of delivery of oxidants (e.g., oxygen and nitrate) via gas and water (Schaetzl and Anderson, 2005). For example, dry and sandy soils will likely be oxic due to rapid exchange of the soil gas with the atmosphere compared to clayey and wet soils. Indeed, all boreholes in the area that show meltwater sand/gravel in the Quaternary sediment package (element 1) displayed oxic colors. However, soil moisture data are not available for this study site. Therefore, we adopted the topographic feature i.e., slope as a surrogate of the relative spatial

365   variability of soil moisture. In general, upslope areas with steeper topography are drier compared to lowland areas with flat slope because of a thinner soil layer, larger depth to the groundwater table, topography- and gravity-driven redistribution of

moisture, and/or faster evaporation due to higher total input of solar radiant in the upslope area (e.g. Famiglietti et al., 1998; Hawley et al., 1983; Tromp-van Meerveld and McDonnell, 2006). The probabilities used to translate the geological surface map into soft redox surface data hence differs between the steeper sloped Quaternary sequence of Geological Element 1 and

370   the flatter appearance of the buried valley infill of Geological Element 2.

Since borehole information is available for the Quaternary sequence, the sediment color data associated with the lithological samples from the upper parts of the boreholes are used to obtain the translational probabilities (Table 3). Although the sediment colors of all the meltwater sand/gravel indicate oxic conditions, we conservatively attribute oxic conditions with 0.95

375   probability and reducing with 0.05 probability not to eliminate the possibility of reducing conditions in the coarse-grained meltwater deposits. For the buried valley, which is located in the flat lowland, the translational probability of oxic conditions of the Quaternary sequence area were multiplied by a slope factor of 0.3 and that of the reducing values were increased by a slope factor of 1.2. These values were arbitrarily chosen in a conservative manner, such that the resulting probabilities were more equally distributed between the three categories, i.e. softer, than for the Quaternary sequence. Reduced conditions were

380   calculated as the leftover when summing to one over all three redox categories.

Table 3: The soft probabilities for redox (oxic, reducing and reduced) at the surface on the combination of soil texture and topography. The probabilities for each lithology sums to one.

	TI1: Southern Quaternary sequence			TI2: Northern buried valley		
Lithology group	Oxic	Reducing	Reduced	Oxic	Reducing	Reduced
Clay till	0.8	0.20	0	0.24	0.24	0.52
Meltwater sand/gravel	0.95	0.05	0	0.285	0.06	0.655
Meltwater clay/silt	0.8	0.20	0	0.24	0.24	0.52
Sandy till	0.95	0.05	0	0.285	0.06	0.655
Postglacial	0.65	0.25	0.1	0.195	0.3	0.505
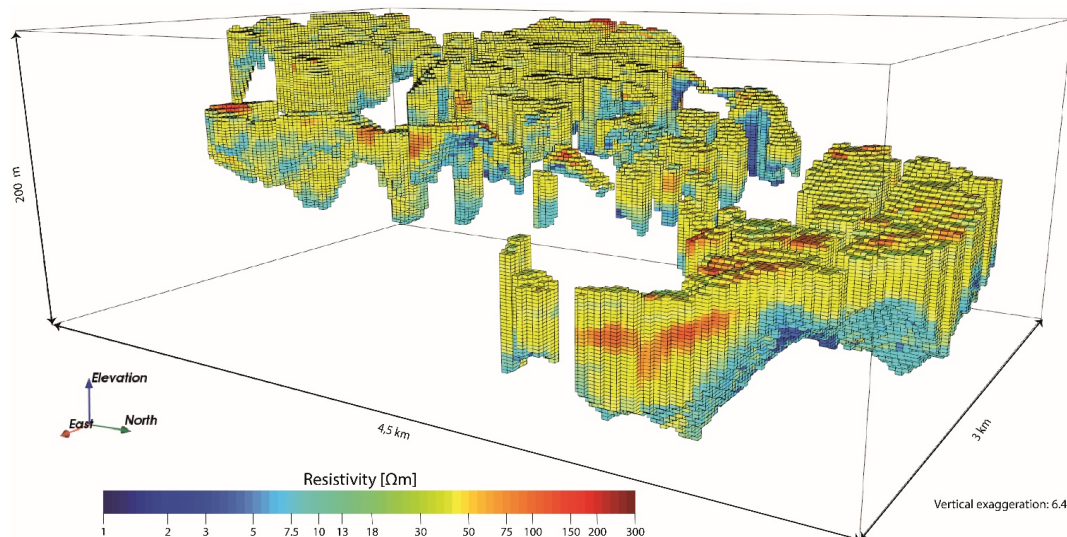
385

Figure 6: 3D resistivity grid from the tTEM model results in a grid equal to the simulation grid.

The tTEM 3D resistivities in the simulation grid contains 87547 voxels covering 43.5 % of the simulation grid (Figure 6). The tTEM 3D resistivity grid is converted into soft probabilities of geology. This requires a known lithology-resistivity relationship, which here is established in two parts. Because the geological training images are based on interpretations of resistivity data

390 in combination with geological information, many voxels in the TIs have a corresponding resistivity value in the resistivity grid. Local histograms for the study area are built for each lithological group by collecting all the resistivity values in the two geology TIs. The final pooled histogram for the two TIs is shown in Figure 7a. Overall, relatively low resistivities are attributed to clay-rich deposits whereas relatively high resistivities are attributed to sandy lithologies, although meltwater accounts for many of the lower resistivities counts. However, the histogram confirms the common issue of lithologies overlapping in the

395 resistivity domain (Barfod et al., 2016; Schamper et al., 2014). The local clay till resistivities are so high that they correspond to much of the meltwater sand/gravel resistivities. The best separation is seen in the meltwater clay/silt category, which tends to have rather low resistivity values. The sandy till is associated with some of the highest resistivity values found in the TI area, whereas the postglacial sediments cover a large spectrum within the most ambiguous resistivity values. For each bin in the histogram, we summarize the size of each lithology group and stack them. If we then normalize with the total number of

400 counts within that resistivity bin we get a cumulative distribution of the lithologies (Figure 7b). Because there are very few counts for the low and high resistivities (<4Ωm and >120Ωm), here defined as <50 counts, we let an a priori established relationship govern these values, consisting of equal probability between the clayey lithology groups for low resistivities and vice versa for sand and high resistivities (Figure 7b). This is based on general observations from Barfod et al. (2016) and Schamper et al. (2014). The obvious difference between the general and local (TI-based) relationship is that meltwater sand

405 can obtain low resistivities using the inferred relationship (Figure 7c). Regardless, the effect of the a priori relationship is miniscule as more than 98.5% of all resistivities in the simulation grid are supported by the inferred relationship. The remaining (<1.5%) is supported solely by the a priori established relationship as seen in the total distribution of all resistivities in the simulation grid Figure 7c.

410
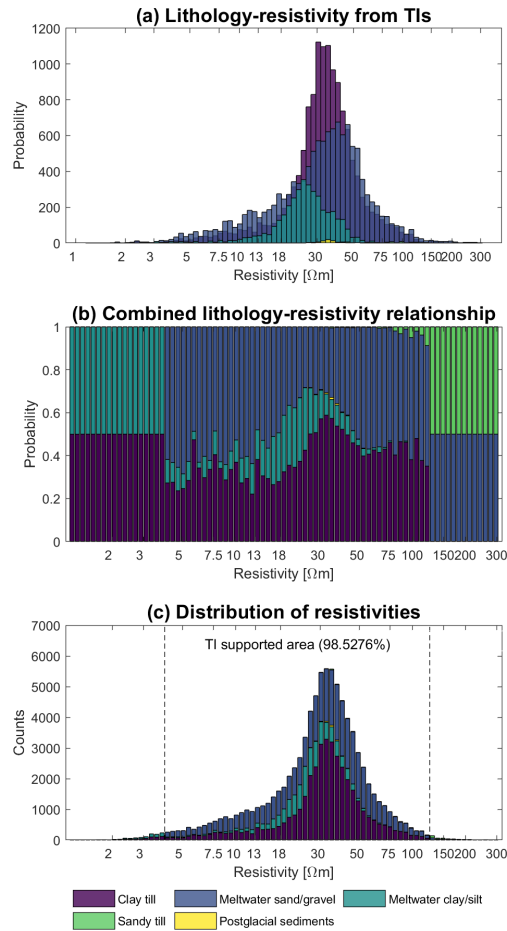
Figure 7: Resistivity-lithology relationships illustrated as a) histogram of resistivity for each lithological group based on the training images (Figure 4) and 3D resistivity grid (Figure 6), b) TI-based cumulative distribution for all lithological groups for each bin and a priori relationship for rare resistivities c) distribution of resistivity values in the full simulation grid (Figure 6) overprinted with the lithology-resistivity relationship in b).

Figure 8 presents the final soft probabilities each of the k lithology classes $p_{tot}(k)$ calculated as:

$$p_{tot}(k) = \frac{p_{sg}(k)p_{tTEM}(k)}{\sum_{k=1}^{K} p_{sg}(k)p_{tTEM}(k)} \qquad (2)$$

where $p_{sg}(k)$ and $p_{tTEM}(k)$ are the soft probabilities from the surface geology and tTEM respectively for each of the K=5 lithologies. The stronger colors at the surface represent the overall certainty level of 0.8 from the surface geology discussed previously. In voxels where soft probability information is available from both tTEM and surface geology, each information is used according to equation 2. The tTEM data is largely more ambiguous in guiding the soft probabilities as evident from the resistivity-lithology relationship in Figure 7 and is mostly within the color range of yellow and red in Figure 8a-c. The dominance of the clay till and meltwater sand/gravel (Figure 8a-b) in the study area are apparent in the soft probabilities when compared to e.g. meltwater clay/silt which is expected primarily in areas of lower resistivities. We do not expect much meltwater clay/silt at the boundary of the modeling domain as portrayed in the training images. The low resistivities of the Paleogene clays at the bottom boundary of the model domain creates this effect. A spatially dependent relationship between resistivity and lithology would remedy such effects. However, the inferred relationship helps guide meltwater sand/silt to lower

430   resistivities and it may not affect the results more than the general uncertainty in the boundary estimate, which depends largely
       on the tTEM resolution. Due to the low count of sandy till and postglacial sediments (Figure 8d-e) in the TIs the probability
       for these lithology classes is considerably lower than the three main classes of the study area. Based on these soft probabilities
       a mode and entropy is calculated and shown in Figure 9. The entropy is clearly lowest at the surface where the soft information
       from the surface geological map is present. Similarly the mode is dominated by the soft information from the surface geological
435   map. Due to the overlapping realtionship in the resistiviy domain (Figure 7), the soft data based on the tTEM data is not as
       informative as at the surface and hence the soft data entropy is higher (yellow color in Figure 9b). The overall pattern in the
       mode model (Figure 9a) reveals a slight tendency to form coherent layers, especially seen in the buried valley. However, in
       many places the mode of the soft data is also raher patchy and changes between small clusters of either meltwater sand or clay
       till.

440
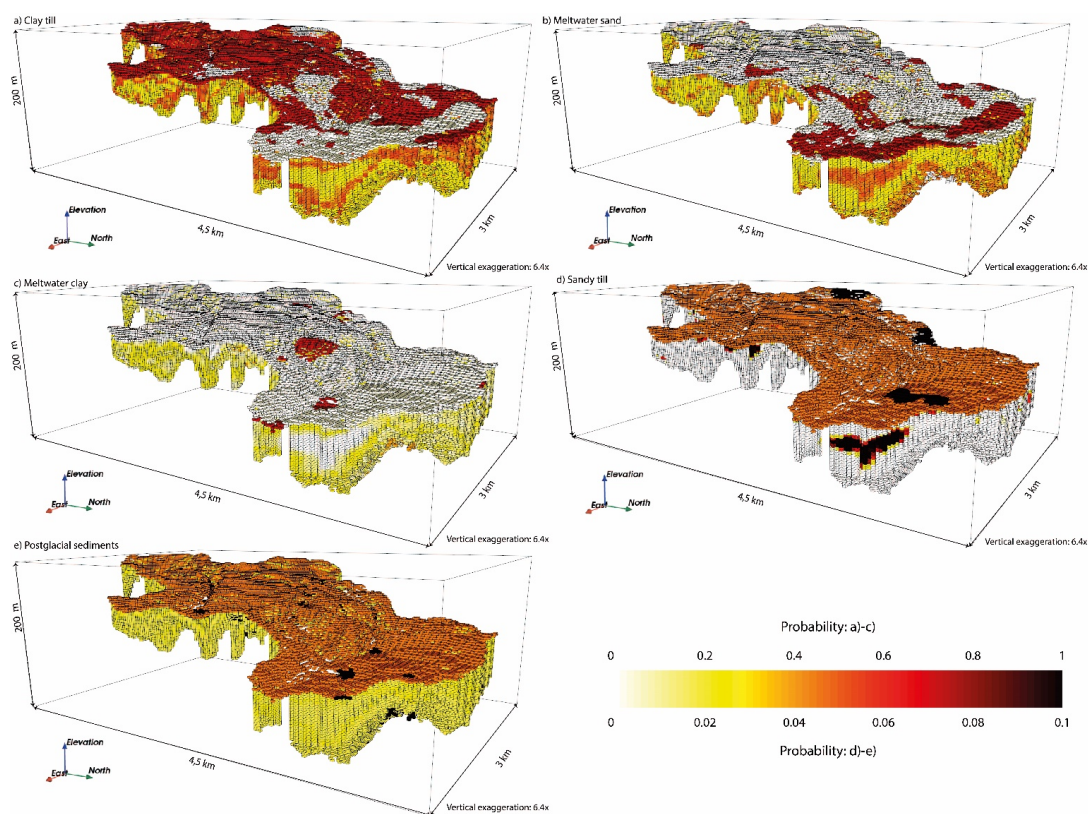
Figure 8: Soft probabilities of geology for the buried valley element. Soft probabilities calculated from the surface geology and tTEM data available. Note the smaller range in the color scale of the sandy till (d) and postglacial sediments (e).
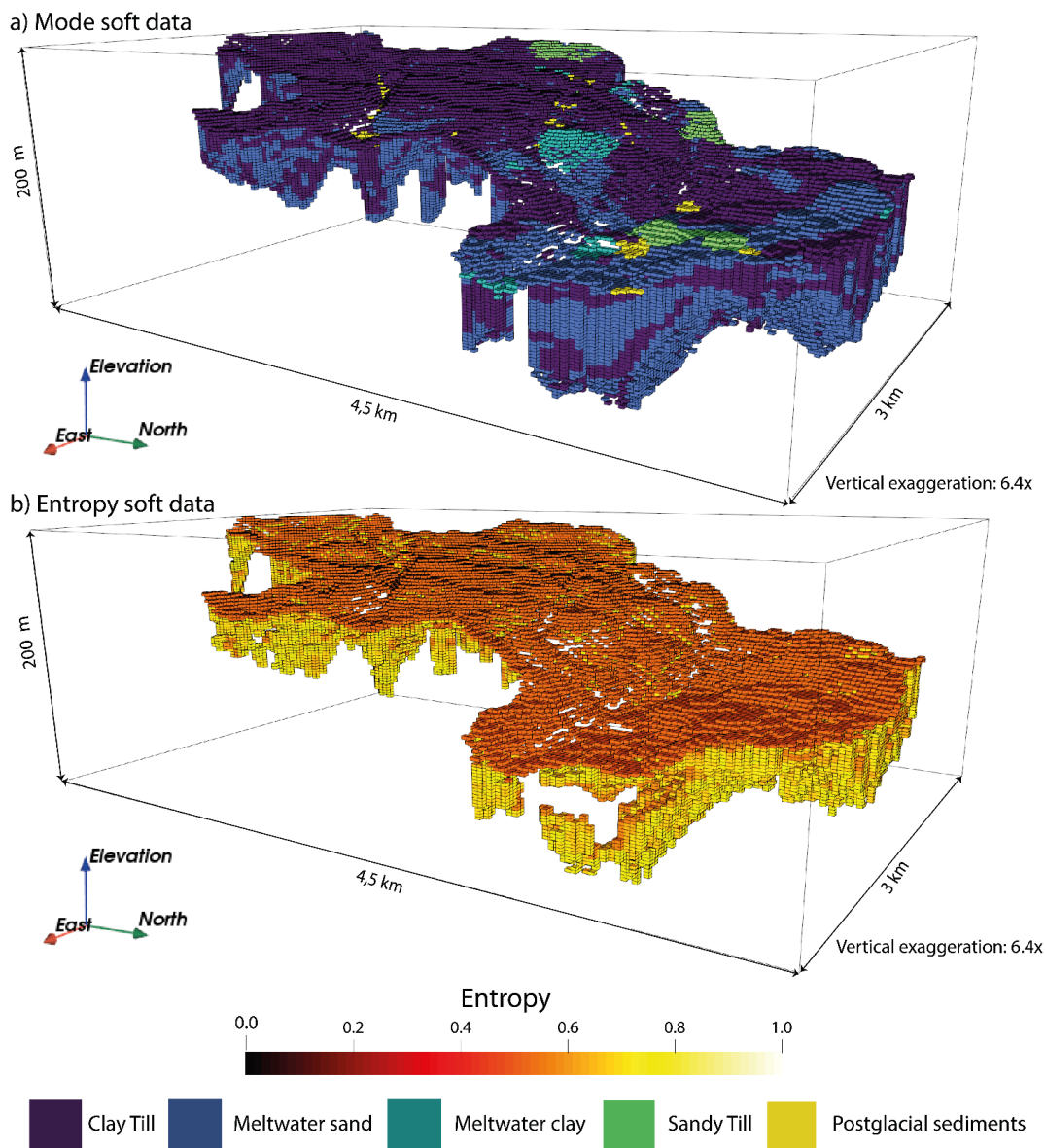
Figure 9: Mode and entropy soft data from Figure 8. Low entropy (certainty) is marked with black color, while white colors represent high entropy (uncertainty).

5.5 Parameterization of the simulation algorithm

In direct sampling, the nodes in the simulation grid are visited sequentially. The training image is consulted at each iteration to find a suitable candidate at each visited node based on already simulated (conditional) nodes. To specify how this procedure is performed, several fundamental parameters need to be set in direct sampling:

- The number of conditional data to take into account when searching the TI influencing the variability. Here, a maximum of 20 neighboring nodes are used which should prevent verbose copying from the TI's happening too often.
- The distance measure determining how well the candidate value match the conditional nodes in the simulation grid. Because both geology and redox are categorical variables we use the number of mismatching nodes as distance

455   measure with a tolerance of 10% mismatch. For 20 neighboring nodes, we hence allow two conditional nodes to differ between the TI and the simulation grid to accept the currently proposed value.

- The maximum number of iterations allowed to find a suitable match within the TI. We allow a scan of the entire TI in order to find a suitable match. If a match is impossible, the candidate providing the lowest misfit is retrieved and "flagged". During post-processing the flagged cells are simulated again to minimize the appearance of simulation

460   artifacts.

- The path at which the simulation grid nodes are visited needs to be selected. We choose a random path as is often used in MPS simulation. The random path have a tendency to underestimate soft data and provide less resolution in the results compared to other path types (Hansen et al., 2018).

6 Modeling results

465   In this section, we present the modeling results from the set of realizations of both geology and redox generated with MPS simulation. Figure 10 shows two such realizations of geology and redox, respectively. The overall geology and redox architecture are in accordance with the TIs. Geological layers are coherent and placed in the correct chronological order, while the redox architecture shows oxic conditions at the surface with increasing reducing conditions at depth. The architecture stays relatively fixed between the realizations, and variability is predominantly small-scale. Given the high amount of conditioning

470   data, this is not unexpected. Occurrences of sole voxels different from the surroundings happens for both variables, albeit rarely. This deviation from the overall pattern of coherent layers is a product of the simulation setup and are as such considered artifacts.
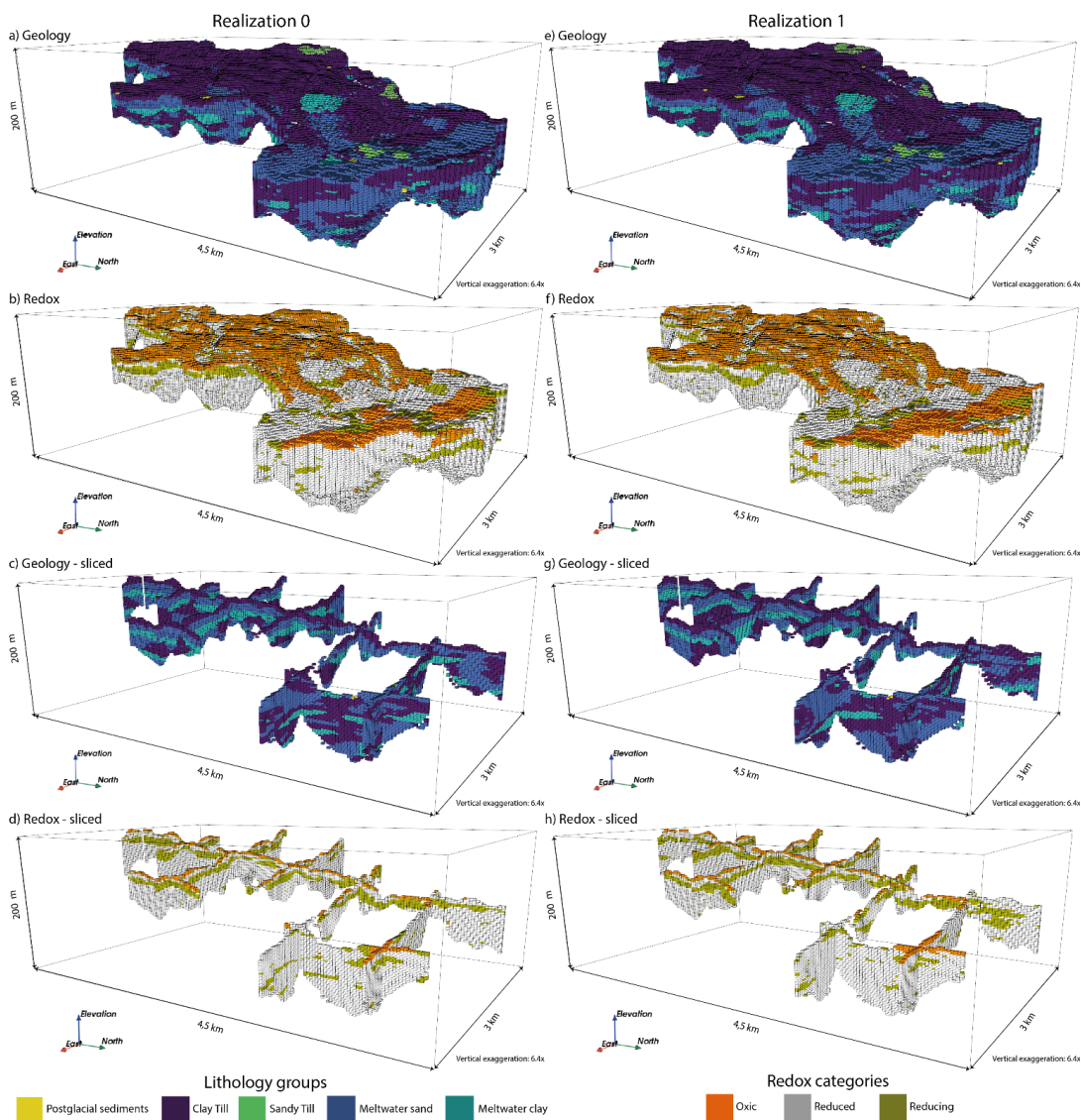
475   **Figure 10: a-b) One realization of jointly simulated geology and redox c-d) The same realization sliced in the X and Y direction. e-h) Same figure configuration as in a-d but for a different realization.**

The main part of the Quaternary sequence element (Geological Element 1) is covered by an approximately 8-10 m thick clay till (Figure 10). Alternating layers of meltwater deposits follow this. Some deposits of sandy till and postglacial sediments are

480 seen at the top of the models. The extent changes during simulation according to the buffer zone. These deposits are rarely deeper than 6 m. The buried valley (Geological Element 2) is mostly covered by a relatively thin layer of meltwater sand followed by clay till and more meltwater sand, respectively. The lateral extent of layers in the buried valley is less than in the Quaternary sequence, as portrayed in the TIs.

485 Due to the joint simulation of geology and redox in the current setup, the overall redox architecture in the realizations is coherent with the geology as outlined in the TI. For example, the TIs indicate that meltwater sand beneath clay till at the surface is located where a thinner reducing zone (green) is expected, which is also the case when comparing e.g. Figure 10c,g with Figure 10d,h. This reducing zone is present in both redox realizations (Figure 10d and Figure 10h) and hence the overall redox architecture is in place, and the difference is mainly small-scale in the extent of this zone. The layered structure of the

490 reducing zone below the reduced zone might be explained by the geological window structure around the sandy till (Figure 10d,h; Kim et al., 2019). Alternatively, unsaturated sand may be situated just below the clay till or both a vertical and horizontal flow is occurring in the meltwater sand. In general, reducing conditions (green) are usually attributed to meltwater sand/gravel in the TIs, which is also the case for the realizations. However, small patches of reducing conditions in the deeper parts of the realizations are unwanted simulation artifacts. Because these are too tiny and surrounded by reduced conditions, we argue that

495 for N-retention simulations these artifacts may be negligible. At the top of the simulation domain, the redox conditions display more variability than the geology, which are heavily influenced by hard data. The clearest example is found at the surface of the buried valley. Meltwater sand/gravel dominates the northernmost part of the simulation domain. The redox conditions at the surface at this location vary significantly between oxic and reducing conditions amongst the realizations. The southernmost part of the buried valley is more stable in the prediction of reduced conditions at the surface, but both reducing and in rare

500 cases also oxic conditions seem to be possible in this area as well.
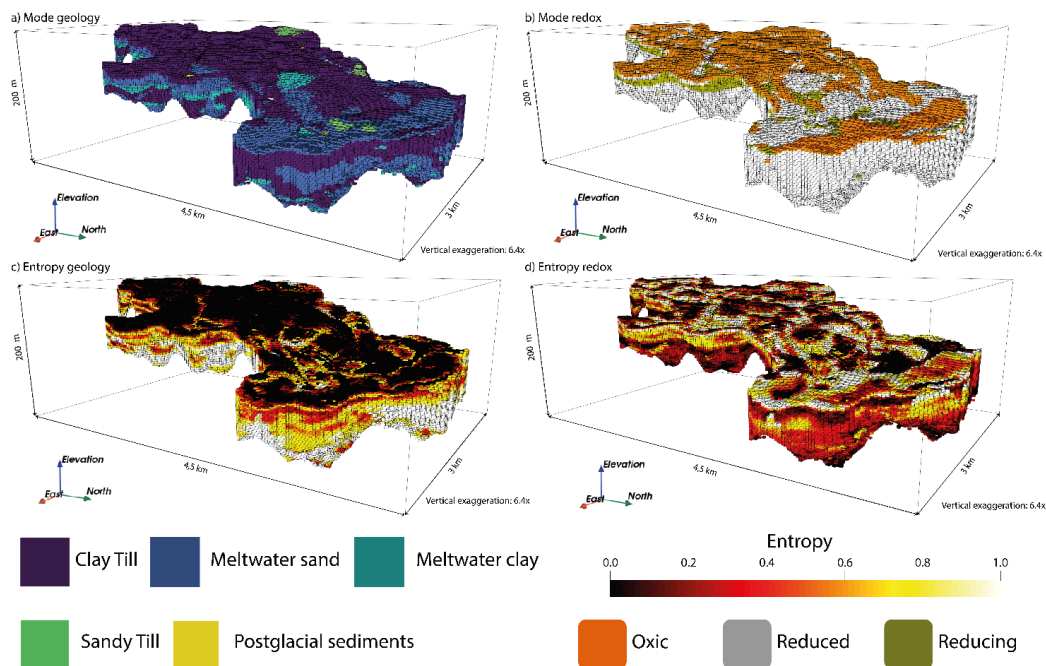
Figure 11: Modes and entropy of 100 geology and redox realizations. Low entropy (certainty) is marked with black color, while white colors represent high entropy (uncertainty).

In total, we simulate 100 realizations similar to those presented in Figure 10. The mode, i.e. the most frequent category within each voxel is presented along the entropy in Figure 11. For example, the low entropy in the surface layer in the geology show that we are certain of the outcome. That outcome is then available in the mode. In this case, the entropy is expected to be close to zero in large parts of surface since this is where most of the hard data is placed directly in the simulation grid. The more uninformed parts of the surface (lighter colors) corresponds to the buffer zone in the hard data. Again, mode gives the most probable outcome in these voxels, but the high entropy tells us that other categories are almost equally probable. This confirms the qualitative results from inspecting the individual realizations. The mode of the geology does not display some of the minor simulation artifacts seen in the individual realizations, because these are averaged out over many realizations. This indicates that simulation artifacts are not reoccurring in simulations and hence no overall bias is found. The effect of introducing MPS via TIs and hard data increases the information content (lowers entropy) of the final models drastically compared to the soft data only (Figure 9). For the lower part of the simulation domain, the situation is reversed, where the posterior realizations show almost zero information content. This means that the mode found in this region is uncertain. The effect of introducing the training image and hard data for the architecture is clearly seen in the coherent structures produced in the posterior mode in contrast to the patchiness of the mode in Figure 9a.

For the redox architecture results, the smoothness of the mode model is apparent when e.g. comparing the continuity of the reducing zone layer (green in Figure 11b) with the individual realizations (Figure 10b,f) that look more fragmented and again the simulation artifacts tend to average out. Even though the TI (Figure 4b) is trying to convey the message of oxic conditions at the surface of the Quaternary sequence, this is not always the case in the realizations as seen in the mode of redox. The reducing or reduced surface conditions are seen in the valleys of the Quaternary sequence (Element 1). This is also visible in the individual realization of Figure 10b,f.

The entropy of redox is showing a reverse pattern to that of geology. The redox entropy is highest near the surface and decreases

530 with increasing depth, especially the buried valley (Figure 11d). Counter intuitively, the largest redox uncertainty is at the top of the model and it decreases with increasing depth. One could expect the highest redox uncertainty at deeper depth because the density of the hard data is much higher near the surface and for the deeper part of the architecture, the geochemical data is rarely available. However, the entropy sharply decreases in the reduced zone beneath the reducing zone. This pattern fits well with the conceptual understanding of the redox structure evolution: oxic conditions are developed as oxidants (e.g., oxygen

535 and nitrate) infiltrate from the root zone to the subsurface where reduced layers are present. Therefore, a redox front propagates downward and under homogeneous conditions with vertical flow of water, it would be unlikely to develop oxic conditions below the redox front. While the spatial heterogeneity of the geological settings of the near surface environments at various scales (pore scale to landscape) has been well documented (e.g. Baveye et al., 2018; Groffman et al., 2009; Sexstone et al., 1985), implying highly heterogeneous redox conditions in the shallower depth. Some of the voxels at the surface of the

540 Quaternary sequence element depart from the overall pattern by having a very low entropy. This trend is likely aided by the soft data giving high probabilities of oxic conditions at the surface. At the surface and down to about 10-20 m of the buried valley, we generally do not know much about the redox conditions as indicated by the white yellowish colors in Figure 11. The more evenly distributed redox soft data probabilities (Table 3) could explain some of this high entropy.
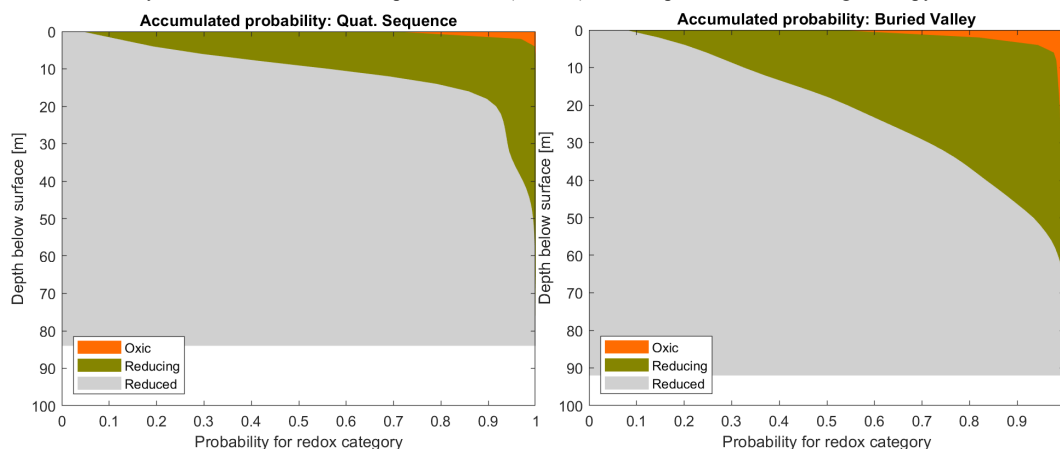
545 **Figure 12: Accumulative probability profiles of redox conditions in the study area. Left: Quaternary sequence, Right: Buried valley.**

The redox conditions can be visualized by plotting the accumulative probability for redox conditions as a function of depth, constructed by summing over all realizations, which hence provides the 1D marginal distribution in all voxels. These marginal distributions are accumulated with depth as shown in Figure 12 for the two geological elements. These are in overall agreement with the geochemical understanding of the study area as just described. Oxic conditions (orange) are primarily found at the

550 surface. Most prominently in the buried valley (right). The reducing conditions (green) are expected primarily in a zone lying 10-20 m below the surface. Finally, reduced conditions dominate the lower parts of simulation area.

7 Discussion

To our knowledge, examples of mapping redox conditions with multiple-point geostatistical simulation are not present. This study sets out with the aim of proposing and reviewing a methodology for modeling both redox architecture and geology
555 simultaneously in high-resolution 3D using MPS. Simulations generally seem to honor both the architecture outlined in the training images and the conditional data available. As pointed out by Tahmasebi (2018), a quantitative evaluation of the performance of MPS is still unresolved, and as previously mentioned, the parameterization could potentially be fine-tuned to produce even better results. However, we adapt the heuristic strategy of Høyer et al., (2017), making sure that the realizations are in accordance with our expectations and focus on presenting the methodology of simulating both geology and redox
560 simultaneously in 3D high-resolution.

7.1 Simulation artifacts

As outlined in the results section, simulation artifacts are occurring in the form of isolated voxels in the deeper part of the simulation grid. For instance, postglacial sediments (yellow, see Figure 10a,e) simulated at unlikely locations, or single voxels of clay till within a unit of meltwater sand (see Figure 10c,g). These artifacts are likely a product of inconsistencies between
565 the prior information and conditioning data. In the current nitrate simulation at the catchment scale, these artifacts do not affect the overall architecture (Figure 11) and redox trends with depth (Figure 12). It is also expected to have negligible impact on hydrological modeling as the overall architecture allows groundwater flow pass by such artifacts. Nevertheless, future studies are required to reduce artifacts of this kind or, at least, downplay their significance. We assume that more rigorous testing of parametrization would reveal insights into a more optimal simulation strategy. In the current setup, post-processing procedures
570 help alleviate some of these simulation artifacts. The flexibility of the current methodology also allows the inclusion of soft probability maps through equation 2 indicating spatial restrictions on certain lithologies or redox conditions, which could remedy some of the deeper lying postglacial sediment artifacts.

A problem related specifically to the study area results is the distribution of redox conditions in the realizations. The TI (Figure
575 4b) is not showing the possibility of reducing conditions at the surface of the buried valley element or reduced conditions at the surface of the Quaternary sequence as seen in the realizations (Figure 10b,f). MPS expects a stationary TI and hence does not consider such information, when looking for a match. In addition, the size of the TI and the features contained within it may not be representative of the whole area. Especially, since the location of TI areas were chosen primarily based on representative geology and good data coverage. If oxic conditions are known to be the only realistic outcome at the surface,
580 this should instead be enforced through conditional data. Rotation in simulation could potentially solve this issue by offering more configurations of oxic conditions to be placed in the valley in the Quaternary sequence. Regardless, from a geochemical perspective, it is reasonable to have reducing or reduced conditions in the valleys, because this is where streams are located in the landscape, leading to high content of organic matter and wetter conditions. In future studies and if a similar approach of TI creation within the simulation domain is chosen, we recommend collaborative efforts between geologists and geochemist in
585 securing the best possible location for representative TIs.

7.2 Resistivity-lithology relationship

The established resistivity-lithology relationship allows us to map the prior probabilities of each lithological group based on the tTEM in the simulation area. Utilizing tTEM as soft data information ensures that it does not have too much influence over
590 the final results. Here, the relationship is inferred from the resistivity grid and training images. When simulating, the general mismatch between the training image patterns (based on interpreted geology) and the tTEM data is thus minimized. Methods

exist for establishing a relationship between resistivity and clay content (Christiansen et al., 2014; Foged et al., 2014). Unfortunately, this is not directly applicable for the lithological groups used here as they are not defined on the basis of the clay content. Alternatively, this relationship could be inferred using boreholes near the study site. Similar to the approach in 595 this study, inferring the resistivity-lithology relationship from boreholes is typically based on deriving probabilities from histograms (Barfod et al., 2016; Gunnink and Siemon, 2015; He et al., 2014a). In accordance with the present results, these studies also show a significant overlap between different lithologies and as such using nearby boreholes for inferring the resistivity-lithology relationship would mainly minimize the reuse of data and avoid subjectivity caried over from the TIs.

7.3 Geological modeling subjectivity and data reuse

The inclusion of geological mapping experts in the creation of TIs introduces modeling subjectivity. Thus, the final realizations could include unverifiable modeling choices following the interpretation procedure in cognitive modeling. Through experiments with geological interpretation of the uncertainty in boreholes, Randle et al. (2019) argued that expert elicitations do not result in accurate predictions of interpretation error. Efforts have been made to make TI generators (Pyrcz et al., 2008) 605 and data-driven TIs without the need for expert knowledge (Vilhelmsen et al., 2019). However, process-based TI generation from expert elicitation is a common approach in MPS applications (Mariethoz and Caers, 2015). A possible explanation for this is the benefit of bringing in prior expert knowledge, which is otherwise difficult to quantify. This ensures that results are in accordance with as much information as possible (Curtis, 2012; Tarantola, 2005) and realizations are not in clear conflict with geological concepts (Jessell et al., 2010; Wellmann and Caumon, 2018).

610

Despite the potential subjectivity in the geological modeling of the study area these modeling choices are primarily guided by data. The tTEM data collected in this study has e.g. contributed to a good correlation between the terrain and the subsurface architectures in the geological interpretations. These observations fit well with the current knowledge of the latest geological events in the area, thus providing good possibilities of making robust geological correlations between the geological and 615 geophysical data.

It might be difficult to quantify the effect of the apparent loss in degrees of freedom that follows from using the same data for establishing the prior information and simulation. In the current study, the problem of reusing data for outlining geological elements, is most likely not critical as only large-scale structural information is partly interpreted from the resistivity data, such 620 as the top of the Paleogene clay layer. The degrees of freedom loss for reusing the resistivity information in the TIs and as conditional data in simulation is undoubtly larger. Although the small size of the TIs may pose a problem for reproducing the intended varibility, in this instance it acts to limit the effect of reusing data. This issue persist for approximately 33% of the total voxels (Table 1).

7.4 Training images and geological elements

If possible, the TI should provide all possible dimensions and shapes of the geological features in the subsurface (Strebelle, 2012). However, sizes of the TIs in the current setup are relatively small compared to the simulation grid and hence do not contain that many configurations. In general, the smaller the TI, the fewer possible structures can be represented (Mariethoz and Caers, 2015). We consider two remedying factors. Firstly, the simplicity of the TI. In the study area, we expect a geology 630 with continuous clay and sand units partly restrained by incised valley structures in the Paleogene clays as seen in Figure 3. Even though the TI is small and simple, it conveys the general pattern to be expected in geological features throughout the simulation domain. The simplicity should alleviate some of this issue, although in an area with more expected heterogeneity,

a more diverse and larger TI would be needed. Secondly, if the geological variability provided in the TI is not sufficient, algorithmically induced variability measures such as scaling and rotation of features is possible with direct simulation
635   (Mariethoz et al., 2010).

The non-stationarity of both sets of TIs is evident. This is a common problem when designing training images directly based on, and mimicking geology, which is inherently non-stationary. This might pose a problem, as only a certain number of the configurations in the TIs will produce a match during the direct simulation. Consequently, we might risk reproducing larger
640   parts of the TI in the realizations. Such verbose copying is partially remedied by the addition of conditioning data and choosing a smaller search radius as argued in Vilhelmsen et al. (2019). However, a smaller search radius comes at a price of not reproducing the features in the TI and adding variability more related to algorithmic choices than geological variability. Luckily, plenty of conditioning data is available for the simulations to remedy some of the shortcomings of the training images. As argued in de Vries et al. (2009), subdividing the TIs and simulation domain into different areas is another possibility to
645   handle non-stationarity. To some degree, the geological elements represents such a subdivision of the entire modeling domain in the study area.

In the current study, we considered the boundaries between the geological elements fixed. In reality, there is some interpretation uncertainty related to these boundaries especially in data scarce areas. Future studies may be able to quantify this uncertainty.
650   If this uncertainty is sufficiently large such that it affects the simulation results significantly, we put forward the idea of re-simulating boundaries between geological elements as part of the simulation.

Because TIs are attributed to a specific geological element, these TIs may be reused in other simulation studies with comparable geological elements and we therefore strongly recommend building a TI library. This approach would alleviate the most
655   fundamental of the issues in the current setups. Information between TI and data becomes independent when using a generalized TI. Specifically, the reuse of data (in constructing the TI and implicitly when inferring the resistivity-lithology relationship) is eradicated. For a smaller geological element, the TIs developed in the study area may also represent a proportionally larger portion of the expected variability. An additional bonus would be a reduction in labor/time since TIs are pre-existing or maybe only need slight alteration.
660

Conceptual TIs or based on data from another study area would most likely be preferable from a geostatistical point of view as it would ensure independence of information. However, in the case of a TI based on nearby data, the TI should be close enough to the study area such that the depositional and redox setting are comparable. Furthermore, the study of Barfod et al. (2018) suggests that TIs become secondary given a high amount of conditional data.
665

7.5 Computationally attractive stochastic simulations

In the current setup, simulations are computationally feasible. 100 realizations of both elements are generated in less than 2.5 hours on a high-end personal laptop (Intel(R) Core(TM) i7-8850H CPU @ 2.60GHz, 6 cores (12 threads) with 10 threads allocated to DeeSse. The average simulation time for a single realization is hence just over 80 seconds. Several factors
670   contribute to this: 1) The relatively small TIs making the number of possible combinations limited, 2) The restriction on maximum 20 conditioning points and 3) the subdivision of the simulation grid into geological elements. Some of the abovementioned factors are algorithm tuning parameters, while others are added bonuses of understanding the geology in question (e.g. the ability of breaking the problem up into smaller bits and choosing an acceptable level of simplicity in the models). In this case, bringing expert field knowledge to the modeling setup is advantageous.

7.6 Multi-purpose modeling results through uncertainties

The proposed workflow allows the quantification of uncertainties in the input data and in the subsurface models. This is a major advantage over e.g. static models. We specifically dealt with prior uncertainty in the geological and redox conditions as portrayed in the TIs and geological map and resistivity data (soft data). Other sources of error (e.g. modeling and measurement errors) in the input data can also be explored, as MPS offers a flexible setup for treating data with uncertainties. Additionally, it is clearly shown in the comparison between mode and entropy of posterior and soft data that MPS adds additional valuable information through the TIs that enable geologically viable architecture. Especially in cases where soft data is too weak to provide significant support. The quantitative description of uncertainties as portrayed by the final ensemble of realizations also has many useful properties for additional analysis. For instance, the ability to produce redox profiles as in Figure 12 is trivial once the simulation is completed. These redox profiles make comparisons with previous studies possible, while offering many other possibilities for summary statistics and quantifying uncertainty. This flexibility in the final analysis is one of the main benefits of applying geostatistical mapping of redox conditions (and geology). With the current methodology, depth profiles can also be calculated for specific sets of x- and y-coordinates to investigate some of the spatial variation in redox. Another example would be to investigate the distribution of redox conditions in the geological groups, which allows assessing new hypotheses on the coupling between geology and redox. It may also reveal insights to the spatial dependencies of such couplings. Entropy gives insight into the nature of information content and therefore it would be an active tool in finding the best spot for further investigation, i.e. showing where information is lacking. For instance, in the case of redox, entropy might be suited for assisting a focused field campaign in retrieving more information of redox in the buried valley element. In the current case, the buried valley showed a lack of information in the first 10-20 meters that is typically critical to model.

From the study area, it seems that it is possible to create a computationally feasible joint stochastic 3D high-resolution model of redox and geology with the current setup. However, these findings cannot be extrapolated directly to other study areas. Future research includes testing the method in other catchment areas to assess the robustness and general applicability. Many improvements, besides fine-tuning algorithm parameters, also exist. We e.g. expect improvements and minor changes to the overall setup, as different study areas will contain site-specific challenges that should be addressed. One of the current issues that need to be adressed is how best to quantify and integrate soft data. Besides the resitivity-lithology relationship, we also recognize the need for an extensive study on the quantification of uncertainty in geological maps such as the geological surface map presented here, but it is beyond the scope of the current study.

8 Conclusion

705 This study sets out to model both redox architecture and geology simultaneously in high-resolution 3D due to the dependency of the evolution of the subsurface redox conditions on the hydrogeological pathways. This is achieved using a bivariate MPS simulation. MPS modeling with a bivariate TI of geology and redox presents some important features compared to previous mapping studies: 1) MPS simulation effectively produces geology and redox following expectations and 2) TIs provide an intuitive and easy collaboration across different fields of expertise. Valuable expert information, otherwise difficult to quantify,

710 is seamlessly integrated within MPS. This ensures in our case that there is a correspondence between geology and redox conditions, which is one of the key strengths of the proposed methodology. Although challenges in the current approach exist, we conclude that the proposed methodology offers improvements to existing methods for mapping geology and redox by producing consistent realizations of both variables. The flexibility of the geostatistical results as represented by the ensemble of realizations allows comparisons with traditional mapping techniques. We interpret and model individual sedimentary layers

715 into coherent packages ('geological elements') that greatly help to guide our simulation results and reduce computation costs. This new mapping technique should aid our understanding of the uncertainties and limitations of our knowledge and data. High-resolution 3D understanding of both redox and geological architecture will likely improve predictions of N retention and water pathways in the subsurface. The generalizability of these results is subject to certain limitations as the proposed workflow is only tested on a single study site. This study lays the groundwork for future research into coupled understanding of geology

720 and redox using MPS simulation. Despite its exploratory nature, this study offers valuable insights into the feasibility of joint geostatistical modeling of redox and geology. Several questions remain to be answered regarding simulation algorithm parameterization and interdependence between different sets of information. The geological and redox architecture simulations might be incorporated in hydrological modeling with N-transport to be used for N-retention mapping of the subsurface important for future more targeted N-regulation of agriculture.

725

Author contribution

RBM, HK and AJK have been primarily in charge of methodology development. The idea of geological elements was conceptualized by PS. Geological modeling was carried out by AJK with assistance of PBS, while HK carried out the geochemical analysis under the assistance of BH. IM and AVC provided valuable insights to geophysical data and models.

730 TMH and TNV provided crucial sparring on geostatistical modeling from an applied and theoretical perspective. RBM developed the model setup and performed the simulations, with quality control on the final realizations by HK, PBS and AJK. RBM prepared the first draft of the manuscript with contributions from all co-authors.

Competing interests

The authors declare that they have no conflict of interest

735 ### Acknowledgements

The authors would like to thank Innovation Fund Denmark (8855-00025B) for sponsoring the Mapfield project (www.mapfield.dk) from which this study emerges.

References

740 Abbaspour, K. C., Yang, J., Maximov, I., Siber, R., Bogner, K., Mieleitner, J., Zobrist, J. and Srinivasan, R.: Modelling hydrology and water quality in the pre-alpine/alpine Thur watershed using SWAT, J. Hydrol., 333(2–4), 413–430, doi:10.1016/j.jhydrol.2006.09.014, 2007.

Auken, E., Christiansen, A. V., Westergaard, J. H., Kirkegaard, C., Foged, N. and Viezzoli, A.: An integrated processing scheme for high-resolution airborne electromagnetic surveys, the SkyTEM system, Explor. Geophys., 40(2), 184–192,
745 doi:10.1071/EG08128, 2009.

Auken, E., Christiansen, A. V., Kirkegaard, C., Fiandaca, G., Schamper, C., Behroozmand, A. A., Binley, A., Nielsen, E., Effersø, F., Christensen, N. B., Sørensen, K., Foged, N. and Vignoli, G.: An overview of a highly versatile forward and stable inverse algorithm for airborne, ground-based and borehole electromagnetic and electric data, Explor. Geophys., 46(3), 223–235, doi:10.1071/EG13097, 2015.

750 Auken, E., Foged, N., Larsen, J. J., Lassen, K. V. T., Maurya, P. K., Dath, S. M. and Eiskjær, T. T.: tTEM - A towed transient electromagnetic system for detailed 3D imaging of the top 70 m of the subsurface, Geophysics, 84(1), E13–E22, doi:10.1190/geo2018-0355.1, 2019.

Barfod, A. S., Møller, I. and Christiansen, A. V.: Compiling a national resistivity atlas of Denmark based on airborne and ground-based transient electromagnetic data, J. Appl. Geophys., 134, 199–209, doi:10.1016/j.jappgeo.2016.09.017, 2016.

755 Barfod, A. S., Vilhelmsen, T. N., Jørgensen, F., Christiansen, A. V., Høyer, A.-S., Straubhaar, J. and Møller, I.: Contributions to uncertainty related to hydrostratigraphic modeling using multiple-point statistics, Hydrol. Earth Syst. Sci., 22(10), 5485–5508, doi:10.5194/hess-22-5485-2018, 2018.

Baveye, P. C., Otten, W., Kravchenko, A., Balseiro-Romero, M., Beckers, É., Chalhoub, M., Darnault, C., Eickhorst, T., Garnier, P., Hapca, S., Kiranyaz, S., Monga, O., Mueller, C. W., Nunan, N., Pot, V., Schlüter, S., Schmidt, H. and Vogel, H.
760 J.: Emergent properties of microbial activity in heterogeneous soil microenvironments: Different research approaches are slowly converging, yet major challenges remain, Front. Microbiol., 9(AUG), 1–48, doi:10.3389/fmicb.2018.01929, 2018.

Blicher-Mathiesen, G., Holm, H., Houlborg, T., Rolighed, J., Andersen, H. E., Carstensen, M. V., Jensen, P. G., Wienke, J., Hansen, B. and Thorling, L.: Landovervågningsoplande 2018. NOVANA. Aarhus Universitet, DCE – Nationalt Center for Miljø og Energi, 241 s. - Videnskabelig rapport nr. 352 (in Danish)., 2019.

765 Bond, C. E.: Uncertainty in structural interpretation: Lessons to be learnt, J. Struct. Geol., 74, 185–200, doi:10.1016/j.jsg.2015.03.003, 2015.

Chilès, J.-P. and Delfiner, P.: Geostatistics, 2nd ed., John Wiley & Sons, Inc., Hoboken, NJ, USA., 2012.

Christiansen, A. V., Foged, N. and Auken, E.: A concept for calculating accumulated clay thickness from borehole lithological logs and resistivity models for nitrate vulnerability assessment, J. Appl. Geophys., 108, 69–77,
770 doi:10.1016/j.jappgeo.2014.06.010, 2014.

Claerbout, J. F., Green, C. and Green, I.: EARTH SOUNDINGS ANALYSIS: Processing versus Inversion, Stanford University., 2004.

Close, M. E., Abraham, P., Humphries, B., Lilburne, L., Cuthill, T. and Wilson, S. R.: Predicting groundwater redox status on a regional scale using linear discriminant analysis, J. Contam. Hydrol., 191, 19–32, doi:10.1016/j.jconhyd.2016.04.006, 2016.

775 Curtis, A.: The science of subjectivity, Geology, 40(1), 95–96, doi:10.1130/focus012012.1, 2012.

Dalgaard, T., Hansen, B., Hasler, B., Hertel, O., Hutchings, N. J., Jacobsen, B. H., Stoumann Jensen, L., Kronvang, B., Olesen, J. E., Schjørring, J. K., Sillebak Kristensen, I., Graversgaard, M., Termansen, M. and Vejre, H.: Policies for agricultural nitrogen management—trends, challenges and prospects for improved efficiency in Denmark, Environ. Res. Lett., 9(11), 115002, doi:10.1088/1748-9326/9/11/115002, 2014.

780 Danielsen, J. E., Auken, E., Jørgensen, F., Søndergaard, V. and Sørensen, K. I.: The application of the transient electromagnetic method in hydrogeophysical surveys, J. Appl. Geophys., 53(4), 181–198, doi:10.1016/j.jappgeo.2003.08.004, 2003.

Ernstsen, V. and von Platen, F.: GEUS Rapport 2014/20: Opdatering af det nationale redoxkort fra 2006., 2014.

Ernstsen, V., von Platen, F. and Jakobsen, P. R.: GEUS Rapport 2008/30: Nitratreduktionsklasser for kystnære arealer ("hvide områder") - data og metode. Supplement til GEUS rapport 2006/93., 2008.

785   Famiglietti, J. S., Rudnicki, J. W. and Rodell, M.: Variability in surface moisture content along a hillslope transect: Rattlesnake Hill, Texas, J. Hydrol., 210(1–4), 259–281, doi:10.1016/S0022-1694(98)00187-5, 1998.

Foged, N., Marker, P. A., Christansen, A. V., Bauer-Gottwein, P., Jørgensen, F., Høyer, A.-S. and Auken, E.: Large-scale 3-D modeling by integration of resistivity models and borehole data through inversion, Hydrol. Earth Syst. Sci., 18(11), 4349–4362, doi:10.5194/hess-18-4349-2014, 2014.

790   Goovaerts, P., AvRuskin, G., Meliker, J., Slotnick, M., Jacquez, G. and Nriagu, J.: Geostatistical modeling of the spatial variability of arsenic in groundwater of southeast Michigan, Water Resour. Res., 41(7), 1–19, doi:10.1029/2004WR003705, 2005.

Gravesen, P. and Fredericia, J.: ZEUS-geodatabase system. Borearkivet. Databeskrivelse, kodesystem og sideregistre (In danish)., 1984.

795   Gravey, M. and Mariethoz, G.: Quantile Sampling : a robust and simplified pixel-based multiple-point simulation approach, Geosci. Model Dev., In review, doi:https://doi.org/10.5194/gmd-2019-211, 2019.

Grenthe, I., Stumm, W., Laaksuharju, M., Nilsson, A. C. and Wikberg, P.: Redox potentials and redox reactions in deep groundwater systems, Chem. Geol., 98(1–2), 131–150, doi:10.1016/0009-2541(92)90095-M, 1992.

Groffman, P. M., Butterbach-Bahl, K., Fulweiler, R. W., Gold, A. J., Morse, J. L., Stander, E. K., Tague, C., Tonitto, C. and
800   Vidon, P.: Challenges to incorporating spatially and temporally explicit phenomena (hotspots and hot moments) in denitrification models, Biogeochemistry, 93(1–2), 49–77, doi:10.1007/s10533-008-9277-5, 2009.

Guardiano, F. B. and Srivastava, R. M.: Multivariate Geostatistics: Beyond Bivariate Moments, in Geostatistics Tróia '92. Quantitative Geology and Geostatistics, edited by A. Soares, pp. 133–144, Springer, Dordrecht., 1993.

Gulbrandsen, M. L., Cordua, K. S., Bach, T. and Hansen, T. M.: Smart Interpretation – automatic geological interpretations
805   based on supervised statistical models, Comput. Geosci., 21(3), 427–440, doi:10.1007/s10596-017-9621-8, 2017.

Gunnink, J. L. and Siemon, B.: Applying airborne electromagnetics in 3D stochastic geohydrological modelling for determining groundwater protection, Near Surf. Geophys., 13(1), 45–60, doi:10.3997/1873-0604.2014044, 2015.

Hansen, A. L., Christensen, B. S. B., Ernstsen, V., He, X. and Refsgaard, J. C.: A concept for estimating depth of the redox interface for catchment-scale nitrate modelling in a till area in Denmark, Hydrogeol. J., 22, 1639–1655, doi:10.1007/s10040-
810   014-1152-y, 2014a.

Hansen, B., Sonnenborg, T. O., Møller, I., Bernth, J., Høyer, A.-S., Rasmussen, P., Sandersen, P. B. E. and Jørgensen, F.: Nitrate vulnerability assessment of aquifers, Environ. Earth Sci., 75(12), 999, doi:10.1007/s12665-016-5767-2, 2016a.

Hansen, B., Thorling, L., Schullehner, J., Termansen, M. and Dalgaard, T.: Groundwater nitrate response to sustainable nitrogen management, Sci. Rep., 7: 8566 |(1), 1–12, doi:10.1038/s41598-017-07147-2, 2017.

815   Hansen, B., Thorling, L., Kim, H. and Blicher-Mathiesen, G.: Long-term nitrate response in shallow groundwater to agricultural N regulations in Denmark, J. Environ. Manage., 240(February), 66–74, doi:10.1016/j.jenvman.2019.03.075, 2019.

Hansen, M. and Pjetursson, B.: Free, online Danish shallow geological data, Geol. Surv. Denmark Greenl. Bull., 23, 53–56, doi:https://doi.org/10.34194/geusb.v23.4842, 2011.

Hansen, T. M., Cordua, K. S., Jacobsen, B. H. and Mosegaard, K.: Accounting for imperfect forward modeling in geophysical
820   inverse problems - Exemplified for crosshole tomography, Geophysics, 79(3), H1–H21, doi:10.1190/GEO2013-0215.1, 2014b.

Hansen, T. M., Vu, L. T. and Bach, T.: MPSLIB: A C++ class for sequential simulation of multiple-point statistical models, SoftwareX, 5, 127–133, doi:10.1016/j.softx.2016.07.001, 2016b.

Hansen, T. M., Vu, L. T., Mosegaard, K. and Cordua, K. S.: Multiple point statistical simulation using uncertain (soft)

825   conditional data, Comput. Geosci., 114(2018), 1–10, doi:10.1016/j.cageo.2018.01.017, 2018.

Hawley, M. E., Jackson, T. J. and McCuen, R. H.: Surface soil moisture variation on small agricultural watersheds, J. Hydrol., 62(1–4), 179–200, doi:10.1016/0022-1694(83)90102-6, 1983.

He, X., Koch, J., Sonnenborg, T. O., Jørgensen, F., Schamper, C. and Christian Refsgaard, J.: Transition probability-based stochastic geological modeling using airborne geophysical data and borehole data, Water Resour. Res., 50(4), 3147–3169,

830   doi:10.1002/2013WR014593, 2014a.

He, X. L., Sonnenborg, T. O., Jørgensen, F. and Jensen, K. H.: The effect of training image and secondary data integration with multiple-point geostatistics in groundwater modelling, Hydrol. Earth Syst. Sci., 18(8), 2943–2954, doi:10.5194/hess-18-2943-2014, 2014b.

Hoffimann, J., Scheidt, C., Barfod, A. S. and Caers, J.: Stochastic simulation by image quilting of process-based geological

835   models, Comput. Geosci., 106(February), 18–32, doi:10.1016/j.cageo.2017.05.012, 2017.

Høyer, A.-S., Jørgensen, F., Sandersen, P. B. E., Viezzoli, A. and Møller, I.: 3D geological modelling of a complex buried-valley network delineated from borehole and AEM data, J. Appl. Geophys., 122, 94–102, doi:10.1016/j.jappgeo.2015.09.004, 2015.

Høyer, A.-S., Vignoli, G., Hansen, T. M., Vu, L. T., Keefer, D. A. and Jørgensen, F.: Multiple-point statistical simulation for

840   hydrogeological models: 3-D training image development and conditioning strategies, Hydrol. Earth Syst. Sci., 21(12), 6069–6089, doi:10.5194/hess-21-6069-2017, 2017.

https://eng.geus.dk/products-services-facilities/data-and-maps/maps-of-denmark/: GEUS Maps of Denmark, [online] Available from: https://eng.geus.dk/products-services-facilities/data-and-maps/maps-of-denmark/ (Accessed 25 May 2020), 2020.

845   Jakobsen, P. R., Hermansen, B. and Tougaard, L.: Danmarks digitale jordartskort 1:25000 Version 3.1. Danmark og Grønlands Geologiske undersøgelser rapport no. 40: De nationale geologiske undersøgelser for Danmark og Grønland (In Danish)., 2011.

Jessell, M. W., Aillères, L. and de Kemp, E. A.: Towards an integrated inversion of geoscientific data: What price of geology?, Tectonophysics, 490(3–4), 294–306, doi:10.1016/j.tecto.2010.05.020, 2010.

Jørgensen, F. and Sandersen, P. B. E.: Buried and open tunnel valleys in Denmark-erosion beneath multiple ice sheets, Quat.

850   Sci. Rev., 25(11–12), 1339–1363, doi:10.1016/j.quascirev.2005.11.006, 2006.

Jørgensen, F., Møller, R. R., Nebel, L., Jensen, N. P., Christiansen, A. V. and Sandersen, P. B. E.: A method for cognitive 3D geological voxel modelling of AEM data, Bull. Eng. Geol. Environ., 72(3–4), 421–432, doi:10.1007/s10064-013-0487-2, 2013.

Jørgensen, F., Høyer, A.-S., Sandersen, P. B. E., He, X. and Foged, N.: Combining 3D geological modelling techniques to

855   address variations in geology, data type and density - An example from Southern Denmark, Comput. Geosci., 81, 53–63, doi:10.1016/j.cageo.2015.04.010, 2015.

Journel, A. G. and Huijbregts, C. J.: Mining Geostatistcs, 1st ed., Academic Press, Inc., London., 1989.

Kallis, G. and Butler, D.: The EU water framework directive: Measures and implications, Water Policy, 3(2), 125–142, doi:10.1016/S1366-7017(01)00007-1, 2001.

860   Keaton, J. R. and Degraff, J. V.: Surface observation and geologic mapping, Spec. Rep. - Natl. Res. Counc. Transp. Res. Board, 247(January 1996), 178–230, 1996.

Keefer, D. A.: A Framework and Methods for Characterizing Uncertainty in Geologic Maps, edited by R. H. Thorleifson LHBerg RC, Three Dimens. Geol. Mapp. Groundw. Appl. Minnesota Geol. Surv. Open File Rep., 07--4, 2007.

Kim, H., Høyer, A.-S., Jakobsen, R., Thorling, L., Aamand, J., Maurya, P. K., Christiansen, A. V. and Hansen, B.: 3D

865   characterization of the subsurface redox architecture in complex geological settings, Sci. Total Environ., 693, doi:10.1016/j.scitotenv.2019.133583, 2019.

Koch, J., Stisen, S., Refsgaard, J. C., Ernstsen, V., Jakobsen, P. R. and Højberg, A. L.: Modeling Depth of the Redox Interface

at High Resolution at National Scale Using Random Forest and Residual Gaussian Simulation, Water Resour. Res., 55(2), 1451–1469, doi:10.1029/2018WR023939, 2019.

870 Lee, J., Jang, C., Wang, S., Liang, C. and Liu, C.: Delineation of spatial redox zones using discriminant analysis and geochemical modelling in arsenic-affected alluvial aquifers, Hydrol. Process., 22(16), 3029–3041, doi:10.1002/hyp.6884, 2008.

Lin, Y. P.: Simulating Spatial Distributions, Variability and Uncertainty of Soil Arsenic by Geostatistical Simulations in Geographic Information Systems, Open Environ. Sci., 2(1), 26–33, doi:10.2174/1876325100802010026, 2008.

875 Lindsay, M. D., Aillères, L., Jessell, M. W., de Kemp, E. A. and Betts, P. G.: Locating and quantifying geological uncertainty in three-dimensional models: Analysis of the Gippsland Basin, southeastern Australia, Tectonophysics, 546–547, 10–27, doi:10.1016/j.tecto.2012.04.007, 2012.

Loke, M. H., Chambers, J. E., Rucker, D. F., Kuras, O. and Wilkinson, P. B.: Recent developments in the direct-current geoelectrical imaging method, J. Appl. Geophys., 95, 135–156, doi:10.1016/j.jappgeo.2013.02.017, 2013.

880 Madsen, R. B. and Hansen, T. M.: Estimation and accounting for the modeling error in probabilistic linearized AVO inversion, Geophysics, 83(2), N15–N30, doi:10.1190/geo2017-0404.1, 2018.

Madsen, R. B., Nørmark, E. and Hansen, T. M.: Accounting for Processing Errors in AVO / AVA Data, in 80th EAGE Conference & Exhibition Proceedings, p. 5, EAGE., 2018.

Malinverno, A. and Briggs, V. A.: Expanded uncertainty quantification in inverse problems: Hierarchical Bayes and empirical

885 Bayes, Geophysics, 69(4), 1005–1016, doi:10.1190/1.1778243, 2004.

Mariethoz, G. and Caers, J.: Multiple-point geostatistics: Stochastic modeling with training images, 1st ed., John Wiley & Sons., 2015.

Mariethoz, G., Renard, P. and Straubhaar, J.: The direct sampling method to perform multiple-point geostatistical simulations, Water Resour. Res., 46(11), 1–14, doi:10.1029/2008WR007621, 2010.

890 Mariethoz, G., Straubhaar, J., Renard, P., Chugunova, T. and Biver, P.: Constraining distance-based multipoint simulations to proportions and trends, Environ. Model. Softw., 72(2014), 184–197, doi:10.1016/j.envsoft.2015.07.007, 2015.

Møller, I., Søndergaard, V. H. and Jørgensen, F.: Geophysical methods and data administration in Danish groundwater mapping, Geol. Surv. Denmark Greenl. Bull., 17, 41–44, doi:10.34194/geusb.v17.5010, 2009.

Nolan, B. T., Fienen, M. N. and Lorenz, D. L.: A statistical learning framework for groundwater nitrate models of the Central

895 Valley, California, USA, J. Hydrol., 531, 902–911, doi:10.1016/j.jhydrol.2015.10.025, 2015.

Pyrcz, M. J., Boisvert, J. B. and Deutsch, C. V.: A library of training images for fluvial and deepwater reservoirs and associated code, Comput. Geosci., 34(5), 542–560, doi:10.1016/j.cageo.2007.05.015, 2008.

Randle, C. H., Bond, C. E., Lark, R. M. and Monaghan, A. A.: Uncertainty in geological interpretations: Effectiveness of expert elicitations, Geosphere, 15(1), 108–118, doi:10.1130/GES01586.1, 2019.

900 Ransom, K. M., Nolan, B. T., A. Traum, J., Faunt, C. C., Bell, A. M., Gronberg, J. A. M., Wheeler, D. C., Z. Rosecrans, C., Jurgens, B., Schwarz, G. E., Belitz, K., M. Eberts, S., Kourakos, G. and Harter, T.: A hybrid machine learning model to predict and visualize nitrate concentration throughout the Central Valley aquifer, California, USA, Sci. Total Environ., 601–602, 1160–1172, doi:10.1016/j.scitotenv.2017.05.192, 2017.

Rosecrans, C. Z., Nolan, B. T. and Gronberg, J. A. M.: Prediction and visualization of redox conditions in the groundwater of

905 Central Valley , California, J. Hydrol., 546, 341–356, doi:10.1016/j.jhydrol.2017.01.014, 2017.

Sandersen, P. B. E.: Uncertainty assessment of geological models - A qualitative approach, in Calibration and Reliability in Groundwater Modelling: Credibility of Modelling, edited by J. C. Refsgaard, K. Kovar, E. Haarder, and E. Nygaard, pp. 345–349, IAHS Redbook ModelCARE 2007., 2008.

Sandersen, P. B. E. and Jørgensen, F.: Kortlægning af begravede dale i Danmark (Mapping of Buried Valleys in Denmark),

910 Opdatering 2015 (Update 2015). Volumes 1 & 2 (In Danish), GEUS Special Publication., 2016.

Sandersen, P. B. E. and Jørgensen, F.: Buried tunnel valleys in Denmark and their impact on the geological architecture of the subsurface, Geol. Surv. Denmark Greenl. Bull., 38, 13–16, doi:https://doi.org/10.34194/geusb.v38.4388, 2017.

Sandersen, P. B. E., Jørgensen, F., Larsen, N. K., Westergaard, J. H. and Auken, E.: Rapid tunnel-valley formation beneath the receding Late Weichselian ice sheet in Vendsyssel, Denmark, Boreas, 38(4), 834–851, doi:10.1111/j.1502-3885.2009.00105.x, 2009.

915   Schaetzl, R. J. and Anderson, S.: Basic concepts: soil physics, in Soils, pp. 82–92, Cambridge University Press., 2005.

Schamper, C., Jørgensen, F., Auken, E. and Effersø, F.: Assessment of near-surface mapping capabilities by airborne transient electromagnetic data — An extensive comparison to conventional borehole data, GEOPHYSICS, 79(4), B187–B199, doi:10.1190/geo2013-0256.1, 2014.

920   Schullehner, J., Hansen, B., Thygesen, M., Pedersen, C. B. and Sigsgaard, T.: Nitrate in drinking water and colorectal cancer risk: A nationwide population-based cohort study, Int. J. Cancer, 143(1), 73–79, doi:10.1002/ijc.31306, 2018.

Sexstone, A. J., Revsbech, N. P., Parkin, T. B. and Tiedje, J. M.: Direct Measurement of Oxygen Profiles and Denitrification Rates in Soil Aggregates, Soil Sci. Soc. Am. J., 49(3), 645–651, doi:10.2136/sssaj1985.03615995004900030024x, 1985.

Shannon, C. E.: A Mathematical Theory of Communication, Bell Syst. Tech. J., 27(4), 623–656, doi:10.1002/j.1538-7305.1948.tb00917.x, 1948.

925   7305.1948.tb00917.x, 1948.

Sørensen, K. I. and Auken, E.: SkyTEM - a new high-resolution helicopter transient electromagnetic system, Explor. Geophys., 35(3), 194–202, doi:10.1071/EG04194, 2004.

Straubhaar, J.: DeeSse User ' s Guide., 2019.

Straubhaar, J., Renard, P., Mariethoz, G., Froidevaux, R. and Besson, O.: An improved parallel multiple-point algorithm using

930   a list approach, Math. Geosci., 43(3), 305–328, doi:10.1007/s11004-011-9328-7, 2011.

Strebelle, S.: Conditional Simulation of Complex Geological Structures Using Multiple-Point Statistics, Math. Geol., 34(1), 1–21, doi:10.1109/CEC.2011.5949612, 2002.

Strebelle, S.: Multiple-Point Geostatistics : from Theory to Practice, in Expanded Abstract Collection from Ninth International Geostatistics Congress, pp. 1–65., 2012.

935   Styrelsen for Dataforsyning og Effektivisering: Danmarks Højdemodel , DHM / Terræn. Data version 2.0 - Januar 2015 (In danish). [online] Available from: https://www.kortforsyningen.dk/sites/default/files/dk_dhm_terraen_v2_1_aug_2016.pdf, 2016.

Tahmasebi, P.: Multiple Point Statistics: A Review, in Handbook of Mathematical Geosciences, pp. 613–643, Springer International Publishing, Cham., 2018.

940   Tahmasebi, P., Hezarkhani, A. and Sahimi, M.: Multiple-point geostatistical modeling based on the cross-correlation functions, Comput. Geosci., 16(3), 779–797, doi:10.1007/s10596-012-9287-1, 2012.

Tarantola, A.: Inverse problem theory and Methods for Model Parameter Estimation, 1st ed., SIAM., 2005.

Temkin, A., Evans, S., Manidis, T., Campbell, C. and Naidenko, O. V.: Exposure-based assessment and economic valuation of adverse birth outcomes and cancer risk due to nitrate in United States drinking water., Environ. Res., 176(December 2018),

945   1–14, doi:10.1016/j.envres.2019.04.009, 2019.

Tesoriero, A. J., Terziotti, S. and Abrams, D. B.: Predicting Redox Conditions in Groundwater at a Regional Scale, Environ. Sci. Technol., 49(16), 9657–9664, doi:10.1021/acs.est.5b01869, 2015.

Thomsen, R., Søndergaard, V. H. and Sørensen, K. I.: Hydrogeological mapping as a basis for establishing site-specific groundwater protection zones in Denmark, Hydrogeol. J., 12(5), 550–562, doi:10.1007/s10040-004-0345-1, 2004.

950   Tromp-van Meerveld, H. J. and McDonnell, J. J.: On the interrelations between topography, soil depth, soil moisture, transpiration rates and species distribution at the hillslope scale, Adv. Water Resour., 29(2), 293–310, doi:10.1016/j.advwatres.2005.02.016, 2006.

Vest Christiansen, A. and Auken, E.: A global measure for depth of investigation, GEOPHYSICS, 77(4), WB171-WB177,

doi:10.1190/geo2011-0393.1, 2012.

955   Viezzoli, A., Christiansen, A. V., Auken, E. and Sørensen, K.: Quasi-3D modeling of airborne TEM data by spatially constrained inversion, GEOPHYSICS, 73(3), F105–F113, doi:10.1190/1.2895521, 2008.

Viezzoli, A., Jørgensen, F. and Sørensen, C.: Flawed processing of airborne em data affecting hydrogeological interpretation, GroundWater, 51(2), 191–202, doi:10.1111/j.1745-6584.2012.00958.x, 2013.

Vilhelmsen, T. N., Auken, E., Christiansen, A. V., Barfod, A. S., Marker, P. A. and Bauer-Gottwein, P.: Combining Clustering
960   Methods With MPS to Estimate Structural Uncertainty for Hydrological Models, Front. Earth Sci., 7(July), 1–15, doi:10.3389/feart.2019.00181, 2019.

de Vries, L. M., Carrera, J., Falivene, O., Gratacós, O. and Slooten, L. J.: Application of multiple point geostatistics to non-stationary images, Math. Geosci., 41(1), 29–42, doi:10.1007/s11004-008-9188-y, 2009.

Wellmann, F. and Caumon, G.: 3-D Structural geological models: Concepts, methods, and uncertainties, 1st ed., Elsevier Inc.,
965   2018.

Wellmann, J. F., De La Varga, M., Murdie, R. E., Gessner, K. and Jessell, M. W.: Uncertainty estimation for a geological model of the Sandstone greenstone belt, Western Australia - insights from integrated geological and geophysical inversion in a Bayesian inference framework, Geol. Soc. Spec. Publ., 453(1), 41–56, doi:10.1144/SP453.12, 2018.

Wilkin, R. T., Barnes, H. L. and Brantley, S. L.: The size distribution of framboidal pyrite in modern sediments, Geochim.
970   Cosmochim. Acta, 60(20), 3897–3912, 1996.

Wilson, S. R., Close, M. E. and Abraham, P.: Applying linear discriminant analysis to predict groundwater redox conditions conducive to denitrification, J. Hydrol., 556, 611–624, doi:10.1016/j.jhydrol.2017.11.045, 2018.

www.buriedvalleys.dk: Buried Valleys, [online] Available from: https://buriedvalleys.dk/ (Accessed 25 May 2020), 2020.

Wycisk, P., Hubert, T., Gossel, W. and Neumann, C.: High-resolution 3D spatial modelling of complex geological structures
975   for an environmental risk assessment of abundant mining and industrial megasites, Comput. Geosci., 35(1), 165–182, doi:10.1016/j.cageo.2007.09.001, 2009.

Yan, S., Liu, Y., Liu, C., Shi, L., Shang, J., Shan, H., Zachara, J., Fredrickson, J., Kennedy, D., Resch, C. T., Thompson, C. and Fansler, S.: Nitrate bioreduction in redox-variable low permeability sediments, Sci. Total Environ., 539, 185–195, doi:10.1016/j.scitotenv.2015.08.122, 2016.

980